Nonlinear dynamics of dual-frequency-pumped multiwave mixing in optical fibers

S. Trillo and S. Wabnitz
Fondazione Ugo Bordoni, Via B. Castiglione 59, 00142 Roma, Italy

T. A. B. Kennedy
School of Physics, Georgia Institute of Technology, Atlanta, Georgia 30332-0430
(Received 26 July 1993; revised manuscript received 27 December 1993)

We investigate the nonlinear dynamics of dual-frequency-pumped four-wave mixing in both the normal- and the anomalous-dispersion regime of optical fibers. We compare the exactly integrable dynamics of a truncated system of nonlinear ordinary differential equations for the first four modes of the multiwave mixing interaction with the phase-plane projections of the numerical solutions of the nonlinear Schrödinger equation.

PACS number(s): 42.65.Hw, 05.45.+b, 42.50.Rh, 42.65.Re

I. INTRODUCTION

Electromagnetic waves at different frequencies parametrically mix in nonlinear optical media thereby generating new frequencies. Among media with cubic nonlinearity optical fibers are ideal candidates for investigating parametric mixing. Although strong conversion has been reported in the experiments [1], early theoretical studies [2] were limited to the linearized (i.e., weak conversion) regime of the interaction. With this assumption, the growth of frequency components at the expense of one or more pump waves is analyzed in terms of coupled linear ordinary differential equations and pump depletion is neglected. This approach may be appropriate in the limit of relatively low pump powers or, equivalently, large difference of phase velocities between the waves, which leads to a mismatched interaction with moderate amounts of frequency conversion. This is the usual situation that occurs in fibers whenever strictly monochromatic waves are considered. In fact, in this case the presence of the stimulated Brillouin scattering (SBS) [3] for input powers above a certain threshold value leads to pump depletion and prevents the observation of a large amount of frequency conversion in the fiber. On the other hand, whenever pulsed or modulated waves are used, the SBS threshold may considerably grow and large frequency conversions are then possible. Note that, although in the following theoretical analysis we will consider for simplicity monochromatic waves and neglect SBS, the results that we obtain are still valid for example with relatively long pulsed pumps; that is, whenever the pump pulse time width is long when compared with the inverse frequency separation between the pump channels. In order to assess the impact of four-wave mixing as a basic limitation to the operation of fiber-based telecommunication systems [4–8], one should consider the so-called strong-interaction regime [9–11], where the input power in adjacent wavelength channels is relatively high and the frequency separation between the channels is kept to a minimum value.

In single-mode fibers, the investigation of four-wave mixing with depleted pumps may be achieved by numerically solving the nonlinear Schrödinger (NLS) equation that governs the wave interaction process (under certain assumptions that limit the applicability of this equation). Although numerical solutions may be easily obtained with standard procedures, an important insight in the mixing process that may be important in the design of telecommunication systems may be provided by the availability of exact solutions. Analytical solutions of the NLS equation for time confined or periodic initial conditions are available in principle by the inverse scattering method [12,13]. Nevertheless, a simple physical insight into the main dynamical properties of the parametric process (e.g., the spatial period of the frequency conversion) may be obtained by assuming that the qualitative properties of the solutions may be described by truncating the field envelope to a small number of frequency components [14]. Indeed, it has been shown that, under certain restrictive conditions, an integrable three-mode truncation may satisfactorily describe the nonlinear dynamics of the modulational instability of a single wave in a fiber [15–18]. The simple one-dimensional truncated system may mimic the dynamics that is associated with the homoclinic manifolds of the infinite dimensional NLS partial differential equation (PDE) [19–22]. Moreover, mode truncations are also capable of providing an accurate description of the dynamical behavior of the numerical solutions of nonintegrable PDE's, such as for example the two coupled NLS equations that govern pulse propagation in a birefringent fiber [23,24] or the driven-damped NLS equation that describes the operation of a modulational instability fiber laser [16,25].

In this work, we consider the multiwave mixing process that is pumped by two monochromatic waves at different frequencies in a single-mode optical fiber. We show that the nonlinear process of energy exchange among four equally spaced and symmetric frequency components of the field (i.e., two equally intense pumps and their first order sidebands) is exactly solvable in terms of Jacobian elliptic functions. This finding rules out the possibility

of chaotic evolutions in the symmetric (or antisymmetric) four-wave mixing process. Note, however, that the presence of any asymmetries, such as for example unequal pump amplitudes or third order dispersion, breaks the integrability of the four-wave mixing nonlinear coupled equations, which leads to chaotic power exchange between the waves [26]. We restrict our attention here for simplicity to the symmetric (or antisymmetric) case, which reduces the four-mode problem to the interaction between two waves, the pump, and the sideband mode. We are interested in the characterization of spatial instabilities in this two mode integrable model. We intend to explore the relationship between these instabilities and the chaotic behavior that is observed in truncations that involve a number of modes that is larger than two [27–32]. Moreover, we consider the effect of the size of the mode truncation by means of the comparison between the four-mode dynamics and the behavior of the numerical solutions of the NLS equation. Clearly these numerical solutions permit to include, in principle, an arbitrarily large number of frequency modes. Based on the complete integrability of the NLS equation, one would then expect (and indeed find [33]) that the chaotic behavior of the finite-dimensional models tends to disappear as the size of the truncation grows larger. Nevertheless, as we shall see, the numerical solutions of the NLS equation still exhibit a complex multiperiodic exchange of energy among several frequencies. This irregular behavior, if it is not strictly speaking chaotic, definitely lies at the borderline of chaos and it is worth further investigations, for example by means of the spectral transform method as it was done in Ref. [34].

In order to make contact with previous work, let us recall that the modulational instability that is induced in a fiber by two intense pump waves that interact through cross-phase modulation was earlier discussed in Ref. [35]. In that work, the coupled NLS equations that represent the nonlinear propagation of the field for frequencies close to the frequencies of the pumps are considered. This description is valid in the limit of large frequency separation (or phase velocity mismatch) between the pumps. In this case, four-wave mixing may be neglected. We consider here the opposite limit, namely the case where the frequency separation (and the phase mismatch) between the pumps is relatively small. The symmetric (or antisymmetric) dual-frequency input pump propagates either in the normal or in the anomalous dispersion regime of the fiber. We include in the analysis a sideband seed of arbitrary relative intensity and phase. It has been shown that, whenever the description of this four-wave mixing process is based on coupled ordinary differential equations (ODE's) involving three sideband pairs (including the pumps in this count), periodic energy exchange between the waves occurs at low powers [30–32]. Whereas as the pump input power is increased, the energy exchange becomes doubly periodic and eventually spatially chaotic. On the other hand, we show here that the truncation to just two sideband pairs may be reduced to an integrable Hamiltonian flow on the plane [36]. Therefore, with a four-wave truncation chaos is absent. Nevertheless, the presence of spatial instabilities that are associated with homoclinic trajectories in the phase plane is closely related to the birth of chaos whenever perturbations are included in the model [37].

In the final section of this paper, we discuss the applicative relevance of the present analysis by pointing out the conditions for the experimental observability of the wave mixing instabilities. We further briefly outline by means of specific examples what is the influence of four-wave mixing as a possible source of deterioration of the performances of wavelength multiplexed optical fiber transmission systems with both distributed or lumped periodic amplification. On the other hand, we discuss how multiwave mixing in the anomalous dispersion regime may be exploited for the generation of short optical pulses.

II. TRUNCATED EQUATIONS

In a single-mode optical fiber the nonlinear propagation of the envelope u of the electric field at the mean frequency ω_0 is described, in dimensionless units, by the NLS equation

$$i\frac{\partial u}{\partial \xi} - \frac{\mathrm{sgn}(k'')}{2}\frac{\partial^2 u}{\partial \tau^2} + |u|^2 u = 0, \tag{1}$$

where $k'' = d^2k/d\omega^2$ is the group-velocity dispersion at the mode at frequency ω_0. Whereas $\xi = z|k''|/t_0^2 \equiv z/z_0$ and $\tau = (t - z/v_g)/t_0$ are the dimensionless propagation distance and time. Here t_0 is an arbitrary time unit, and $1/v_g = dk/d\omega$, v_g being the group velocity of the fiber mode at ω_0.

The PDE (1) may be reduced to a finite set of $2K$ coupled ODE's by means of the ansatz

$$u(\xi,\tau) = \sum_{j=-K+1}^{K} A_{2j-1}(\xi) e^{-i(2j-1)\Omega\tau}, \tag{2}$$

where the A_j are the complex amplitudes of the frequency components of the field and 2Ω is the frequency spacing between these spectral components. One obtains

$$\frac{dA_{2j-1}}{d\xi} + \frac{\mathrm{sgn}(k'')}{2}((2j-1)\Omega)^2 A_{2j-1} + \sum_{l,m=-K+1}^{K} A_{2l-1}A_{2m-1}A^*_{2l-1+2m-1-(2j-1)} = 0. \tag{3}$$

Let us consider the symmetric four-mode ansatz with $A_1 = A_{-1} \equiv A_p/\sqrt{2}$, $A_3 = A_{-3} \equiv A_s/\sqrt{2}$. In other words, we set

$$u(\xi,\tau)=\frac{A_s(\xi)}{\sqrt{2}}\left(e^{-i3\Omega\tau}+e^{i3\Omega\tau}\right)+\frac{A_p(\xi)}{\sqrt{2}}\left(e^{-i\Omega\tau}+e^{i\Omega\tau}\right). \tag{4}$$

The Fourier transform of Eq. (4) is schematically shown in Fig. 1. Note that we take as a reference frequency ω_0 the frequency which is intermediate between the two pumps. Equations (3) reduces to

$$\begin{aligned}-i\frac{dA_p}{d\xi}&=\mp\frac{1}{2}\Omega^2A_p+\left[\frac{3}{2}|A_p|^2+2|A_s|^2\right]A_p+A_s^2A_p^*+|A_p|^2A_s+\frac{A_p^2A_s^*}{2}=\frac{\partial H}{\partial A_s^*},\\ -i\frac{dA_s}{d\xi}&=\mp\frac{9}{2}\Omega^2A_s+\left[\frac{3}{2}|A_s|^2+2|A_p|^2\right]A_s+A_p^2A_s^*+\frac{|A_p|^2A_p^*}{2}=\frac{\partial H}{\partial A_p^*},\end{aligned} \tag{5}$$

where the Hamiltonian H reads

$$H=\mp\frac{1}{2}\left[\Omega^2|A_p|^2+9\Omega^2|A_s|^2\right]+\frac{3}{4}\left[|A_p|^4+|A_s|^4\right]+2|A_pA_s|^2+\frac{1}{2}\left(A_s^2A_p^{*2}+A_s^{*2}A_p^2\right)+\frac{|A_p|^2}{2}\left(A_sA_p^*+A_s^*A_p\right). \tag{6}$$

Equations (5) and (6) may be reduced to a one degree of freedom nonlinear oscillator equation by means of a canonical transformation from the two complex variables $u_{p,s}=|u_{p,s}|\exp(i\Phi_{p,s})$ to the two real conjugate variables $\eta\equiv|A_p|^2/P_t$ and $\Phi\equiv\Phi_s-\Phi_p$, where $P_t=|A_p|^2+|A_s|^2$ is the conserved input power. We obtain that η and Φ obey the coupled nonlinear equations

$$\begin{aligned}\frac{d\eta}{d\zeta}&=-2\eta(1-\eta)\sin(2\Phi)-\eta\sqrt{\eta(1-\eta)}\sin(\Phi)=\frac{\partial\tilde{H}}{\partial\Phi},\\ \frac{d\Phi}{d\zeta}&=\frac{1}{2}(\kappa-1)+\eta+(2\eta-1)\cos(2\Phi)+\frac{4\eta-3}{2\sqrt{1-\eta}}\sqrt{\eta}\cos(\Phi)=-\frac{\partial\tilde{H}}{\partial\eta},\end{aligned} \tag{7}$$

where $\zeta=\xi P_t$, $\kappa=8\,\mathrm{sgn}(k'')\Omega^2/P_t$. The new Hamiltonian $\tilde{H}$ reads

$$\begin{aligned}\tilde{H}=&\frac{1}{2}(1-\kappa)\eta-\frac{\eta^2}{2}+\eta(1-\eta)\cos(2\Phi)\\&+\eta\sqrt{\eta(1-\eta)}\cos(\Phi).\end{aligned} \tag{8}$$

Note that with an antisymmetric four-mode ansatz with $A_1=-A_{-1}\equiv A_p/\sqrt{2}$, $A_3=-A_{-3}\equiv A_s/\sqrt{2}$, that is whenever Eq.(4) is transformed into

$$\begin{aligned}u(\xi,\tau)=&\frac{A_s(\xi)}{\sqrt{2}}\left(e^{-i3\Omega\tau}-e^{i3\Omega\tau}\right)\\&+\frac{A_p(\xi)}{\sqrt{2}}\left(e^{-i\Omega\tau}-e^{i\Omega\tau}\right),\end{aligned} \tag{9}$$

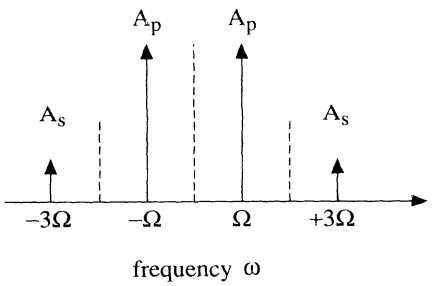

FIG. 1. Schematic illustration of the symmetric four-wave mixing configuration. $A_p(A_s)$ represent the pump (sideband) complex amplitudes. The frequency spacing between the waves is equal to $\Omega'=2\Omega$.

one obtains a reduced Hamiltonian that is identical to (8) except for a minus sign in front of the last term [i.e., the antisymmetric Hamiltonian, say, $\tilde{H}_a$, that corresponds to the ansatz (9) is obtained from Eq. (8) by substituting Φ with $\Phi+\pi$].

III. NONLINEAR EIGENMODES

The fixed points of the finite dimensional system (7) and (8), say, (η_e,Φ_e) represent the nonlinear eigenmodes of the four-wave mixing process. They are defined by setting $d\eta/d\zeta=d\Phi/d\zeta=0$ in Eqs. (7). These points are the extrema of the Hamiltonian (8). Figure 2 shows the dependence of the four-wave mixing eigenmodes on the dimensionless mismatch parameter κ. A simple condition for the vanishing of the right hand side of the first of Eqs. (7) is that $\Phi_e=0$ or $\Phi_e=\pi$. Correspondingly, $\cos(2\Phi_e)=1$ and $\cos(\Phi_e)=\pm1$. From the second of Eqs. (7), one obtains that the fixed points with $\Phi_e=0,\pi$ are the roots of the cubic equation

$$\begin{aligned}&52\eta_e^3+(12\kappa-96)\eta_e^2+(54+\kappa^2-18\kappa)\eta_e\\&\qquad-(9+\kappa^2-6\kappa)=0.\end{aligned} \tag{10}$$

The location of the solutions η_e of Eq. (10) versus the mismatch κ for both $\Phi_e=0$ and $\Phi_e=\pi$ is shown in Fig. (2).

Another fixed point of Eqs. (7) is represented by the

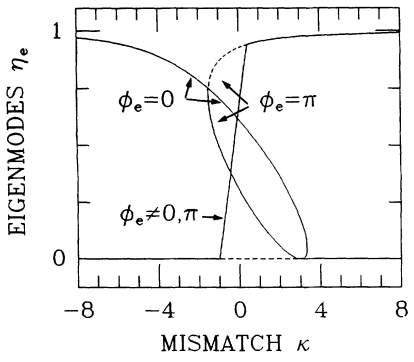

FIG. 2. Bifurcation diagram of the four-wave mixing eigenmodes with coordinates (η_e, Φ_e). Solid (dashed) lines indicate stable (unstable) eigenmodes. The linear mismatch κ is the bifurcation parameter.

sideband mode, that is $\eta_e = 0$, and $\Phi_e = \pm\cos^{-1}[(\kappa - 1)/2]/2$. As can be seen from Fig. 2, this sideband mode is unstable for $-1 < \kappa < 3$. Note that the pump mode is not a fixed point of Eqs. (7), since the sidebands grow from the nonlinear beating of the two pumps also for $A_s(\xi = 0) = 0$. In fact the creation of these sidebands is due to the third-order susceptibility term $\chi^{(3)}(\omega_0 \pm \Omega, \omega_0 \pm \Omega, -(\omega_0 \mp \Omega); -(\omega_0 \pm 3\Omega))$, that leads to the last term in the second of Eqs. (5). The last couple of fixed points is obtained from Eqs. (7) for $\Phi_e \neq n\pi/2$, with n integer, and satisfies

$$\eta_e = \frac{2(1+\kappa)}{3}, \quad \cos^2(\Phi_e) = \frac{1+\kappa}{8(1-2\kappa)}. \tag{11}$$

These fixed points are stable and are shown by the straight line in Fig. 2.

We have determined the stability of the fixed points in Fig. 2 by calculating the second variation of the Hamiltonian $\bar{H}$. Unstable fixed points are shown by dashed lines. Note that in Fig. 2 we have reported the symmetric eigenmodes, i.e., those obtained from the ansatz (4). On the basis of symmetry arguments, we obtain immediately that the nonlinear eigenmodes for the antisymmetric case [see the ansatz in Eq. (9)], are simply obtained from those of Fig. 2 by interchanging Φ with $\Phi + \pi$. In the following section, we will consider the consequence of the bifurcations in Fig. 2 on the topology of the phase-space trajectories of the nonlinear dynamical system (7).

Note that the phase-locked eigensolutions (i.e., the nonlinear eigenmodes with $\Phi_e = 0, \pi$) of the truncated four-mode system (7) provide an approximation to the exact temporal periodic phase-locked traveling-wave solutions of the NLS equation [14,34]. In fact, the temporal profile of the complex amplitude of these periodic time stationary solutions may be expressed in terms of a Jacobian elliptic function. By representing this elliptic function as a discrete Fourier series, one obtains a superposition of phase-locked harmonic waves. Then one may view the four-mode nonlinear eigenmodes as a truncation of the Fourier series of the exact Jacobian function solution. Note that this truncation preserves the correct phase relation between the four waves.

In fact, following the procedure that was outlined in Ref. [34], the traveling-wave solutions of the NLS Eq. (1) may be found by assuming a field of the form $u(\xi,\tau) = |u(\tau+v\xi)|\exp(i\phi)$, where ϕ is a linear function of ξ and τ. For example, in the normal dispersion regime a traveling-wave solution of Eq. (1) (see Ref. [34]) reads

$$u_{t1}(\xi,\tau) = \pm Ak\,\mathrm{sn}(A(\tau+v\xi),k) \times \exp\left\{i\left(v\tau + \xi\frac{(1+k^2)A^2+v^2}{2} + \phi_0\right)\right\}, \tag{12}$$

where $k \in [0,1]$ is the modulus of the elliptic sine function sn, A is an arbitrary amplitude coefficient, v^{-1} is the group velocity of the wave, and ϕ_0 is an arbitrary phase. Considering time periodic solutions with period $2\pi/\Omega$ as we do here, the relationship $v = n\Omega$ (n integer) holds. Moreover, since the function $\mathrm{sn}(x)$ is periodic in x with a period equal to $4K(k)$, where $K(k)$ is the complete elliptic integral of the first kind [38], from Eq. (12) one obtains that the amplitude A is related to the frequency detuning Ω by the relation $A = 2\Omega K(k)/\pi$.

The Fourier series of the elliptic sine in Eq. (12) is formed by the antisymmetric odd harmonics of the frequency detuning Ω [38]. Indeed, one obtains that the truncation of this Fourier series to the first four modes may be approximated by one of the eigenmodes of the Hamiltonian $\tilde{H}_a$. That is, in order to go back from the (η,ϕ) plane to the field u one uses the antisymmetric ansatz (4). In other words, the phase-locked eigensolution u_{t1} in Eq. (12) is approximated by $\hat{u}_{t1}(\tau) = \sqrt{2\eta_e}\sin(\Omega\tau) + \sqrt{2(1-\eta_e)}\exp(i\Phi_e)\sin(3\Omega\tau)$, where η_e is obtained from Eq. (10), and $\Phi_e = 0$.

The same fixed point of $\tilde{H}_a$ (8) in the (η,ϕ) plane has another interpretation in terms of exact phase locked solutions of the NLS equation whenever the symmetric ansatz (4) is employed. In fact, in the normal-dispersion regime Eq. (1) has the additional traveling-wave solution in terms of the Jacobian function cd [38]

$$u_{t2}(\xi,\tau) = \pm Ak\,\mathrm{cd}(A(\tau+v\xi),k) \times \exp\left\{i\left(v\tau + \xi\frac{(1+k^2)A^2+v^2}{2} + \phi_0\right)\right\}. \tag{13}$$

The truncation of the Fourier series expansion of u_{t2} corresponds to the eigenmode of the symmetric Hamiltonian $\tilde{H}$ with the same η_e as before but now $\Phi_e \to \Phi_e + \pi$. In fact, $u_{t2} \simeq \hat{u}_{t2} = \sqrt{2\eta_e}\cos(\Omega\tau) + \sqrt{2(1-\eta_e)}\exp(i\Phi_e)\cos(3\Omega\tau)$, where now $\Phi_e = \pi$.

In the anomalous-dispersion regime, the phase-locked stationary or traveling wave solutions of Eq. (1) are the well-known so-called conoidal waves [14]

$$u_{t3}(\xi,\tau) = \pm Ak\,\mathrm{cn}(A(\tau+v\xi),k) \times \exp\left\{-i\left(v\tau + \xi\frac{(1-2k^2)A^2-v^2}{2} - \phi_0\right)\right\}. \tag{14}$$

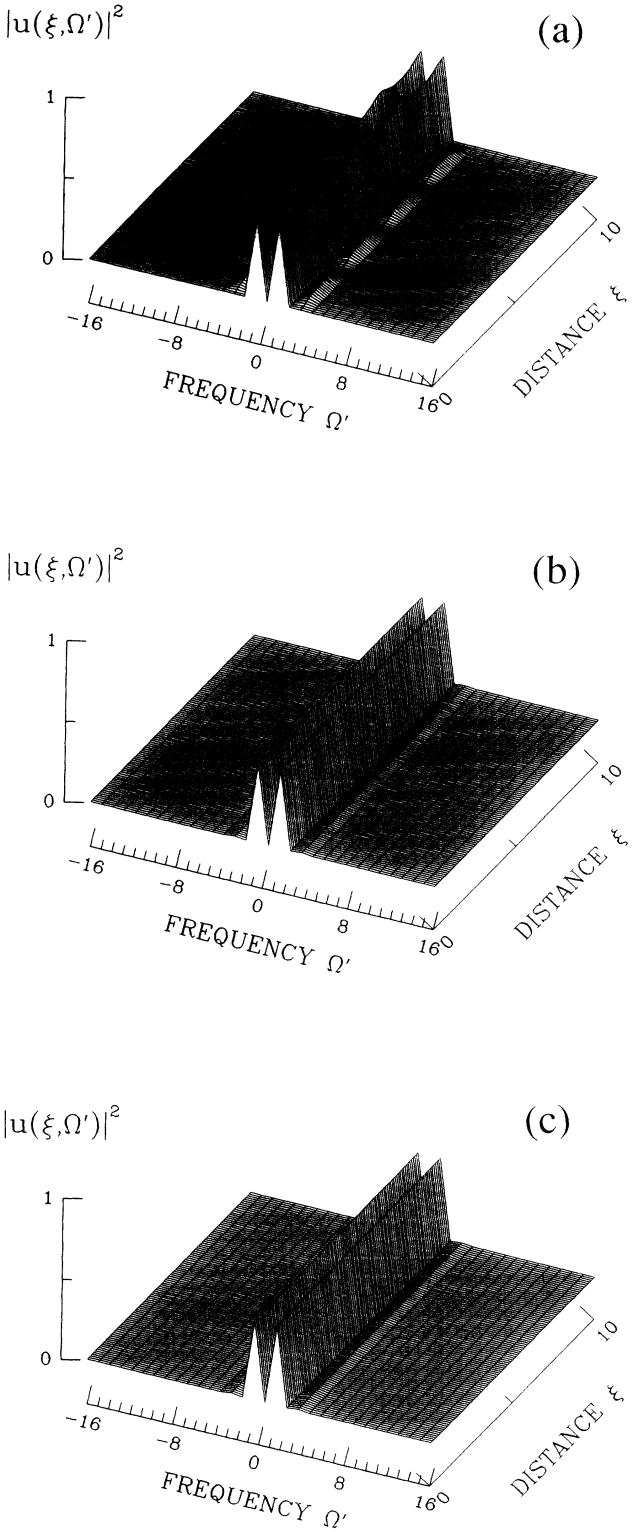

FIG. 3. Power spectrum evolution as obtained from numerical solution of the NLS equation for propagation in the normal-dispersion regime, and $\kappa = 4$. Here the frequency is expressed in units of Ω. (a) In the absence of sideband seed; (b) with initial conditions corresponding to the $\Phi_e = 0$ antisymmetric eigenmode [i.e., the elliptic function sn solution of Eq. (12)]; (c) with initial conditions corresponding to the $\Phi_e = \pi$ symmetric eigenmode [i.e., the elliptic function cd solution of Eq. (13)].

Again in this case the Fourier truncation of u_{t3} may be approximated by an eigenmode of Eqs. (7) with $\Phi_e = 0$ whenever the symmetric ansatz (4) is employed. The exact solution counterpart of this eigenmode, whenever the antisymmetric ansatz (9) is used, involves the Jacobian function sd [38]

$$u(\xi,\tau) = \pm Ak\sqrt{1-k^2}\,\mathrm{sd}(A(\tau+v\xi),k) \times \exp\left\{-i\left(v\tau+\xi\frac{(1-2k^2)A^2+v^2}{2}-\phi_0\right)\right\}. \tag{15}$$

The truncated approximation of this solution is the eigenmode of the antisymmetric Hamiltonian $\tilde{H}_a$ with the same η_e as in the previous case but with $\Phi_e = \pi$.

A detailed investigation of the domain of validity (in terms of the linear mismatch κ) of the four-mode truncation for approximating the exact traveling-wave solutions of the NLS (12)–(15) is beyond the scope of this work. We limit ourselves here to verify that, in the limit of relatively large absolute values of κ, an input condition to the NLS equation that is provided by the fixed points of either $\tilde{H}_a$ or $\tilde{H}$ that we have described above does not lead to appreciable power transfer between the Fourier components, and preserves the phase-locked property of the field. For example, in Fig. 3 we show the evolution with distance ξ of the power spectrum $|\hat{u}(\Omega' = \omega/\Omega)|^2$ that is obtained from the numerical solution of the NLS equation (1) in the normal-dispersion regime. We have set here $\kappa = 4$, that is $\Omega = 1/\sqrt{2}$ with $P_t = 1$.

As can be seen in Fig. 3(a), if the two pumps only are injected at the fiber input, that is whenever $u(0,\tau) = \sqrt{2}\cos(\Omega\tau)$, four-wave mixing leads to a spatially periodic energy conversion into the sidebands at frequency 3Ω. Conversely, Fig. 3(b) shows that by injecting along with the pumps the proper sideband seed the field propagates unchanged, i.e., no frequency conversion occurs. Here we have set $u(0,\tau) = \sqrt{2\eta_e}\sin(\Omega\tau) + \sqrt{2(1-\eta_e)}\sin(3\Omega\tau)$, that corresponds to the eigenmode of the antisymmetric Hamiltonian $\tilde{H}_a$ with $\Phi_e = 0$ and η from Eq. (10) (see also Fig. 2).

Finally, Fig. 3(c) shows that no frequency conversion takes place with a symmetric eigemode at the fiber input. In other words, we have used here the symmetric initial condition $u(0,\tau) = \sqrt{2\eta_e}\cos(\Omega\tau) - \sqrt{2(1-\eta_e)}\cos(3\Omega\tau)$, that corresponds to an eigenmode of $\tilde{H}$ with $\Phi_e = \pi$. Similar results were obtained by solving Eq. (1) in the anomalous-dispersion regime with input conditions that correspond to the antisymmetric eigenmode of $\tilde{H}_a$ with $\Phi_e = 0$ and the symmetric mode of $\tilde{H}$ with $\Phi_e = \pi$.

IV. PHASE-SPACE ANALYSIS

Figures 4 and 5 show the trajectories that represent the solutions of Eqs. (7) in the phase plane $(\eta\cos(\Phi), \eta\sin(\Phi))$ in the normal- and anomalous-dispersion regimes, respectively. Since the Hamiltonian $\tilde{H}$ in Eq. (8) is a conserved quantity along ζ, the trajec-

tories in Figs. 4 and 5 are also the constant level curves of $\tilde{H}$.

Consider first the normal-dispersion regime. Figure 4(a) shows the phase portrait of the four-wave mixing dynamics in the case $\kappa = 4$. As can be seen from Fig. 2, in this case the sideband mode (i.e., the point $\eta_e = 0$) is a stable center. Whereas from Eq. (10) and Fig. 2 one obtains that another stable center exists with $\eta_e \simeq 1$, and $\Phi_e = \pi$. Away from each of the two elliptic fixed points, the representative point of the field moves on stable periodic trajectories. In the case of Fig. 4(a), independently of the input conditions, the relatively large value of the linear mismatch κ leads to a small periodic exchange of energy between the pump and the sidebands.

Figure 4(b) shows that the situation is completely different whenever the mismatch is reduced down to $\kappa = 1$. In fact, in this case the sideband mode is an unstable saddle. Figure 2 shows that the stability of the sideband mode is lost at the bifurcation point $\kappa_e = 3$, where two new stable elliptical fixed points with $\Phi_e = 0, \pi$ appear. As can be seen from the phase-space trajectories in Fig. 4(b), the spatial instability of the sideband mode entails that for $\eta(\zeta = 0) \simeq 1$ and $|\Phi(\zeta = 0)| < \pi/2$, the conversion from the two pumps into the sidebands is greatly enhanced. Moreover, the spatial period of the conversion diverges to infinity on the double loop homoclinic separatrix that emanates from the unstable saddle point with $\eta = 0$.

Figures 4(a) and 4(b) also show a trajectory that originates from the circle with $\eta = 1$ and divides in two distinct regions the motion within the circle. This trajectory is periodically followed by the representative point (η, ϕ) of the field whenever only the two pump lines are injected into the fiber, i.e., the sideband seed is absent at the input. Suppose that the initial point in Fig. 4(b) is located in $(\eta, \phi) = (1, \pi/2)$. The subsequent evolution of this initial condition leads to the point $(\eta, \phi) = (1, 3\pi/2)$ on the unit circle and then back to the initial condition (by moving around the unit circle).

Figure 6 shows the evolution with distance ζ of the power fraction in the pumps, η, and the relative phase ϕ, with an initial condition $\eta = 1$ and $\kappa = 1$ as in Fig. 4(b). The evolution of η and ϕ in this figure may be immediately understood by looking at the corresponding separatrix trajectory in Fig. 4(b). Figure 4(c) (here

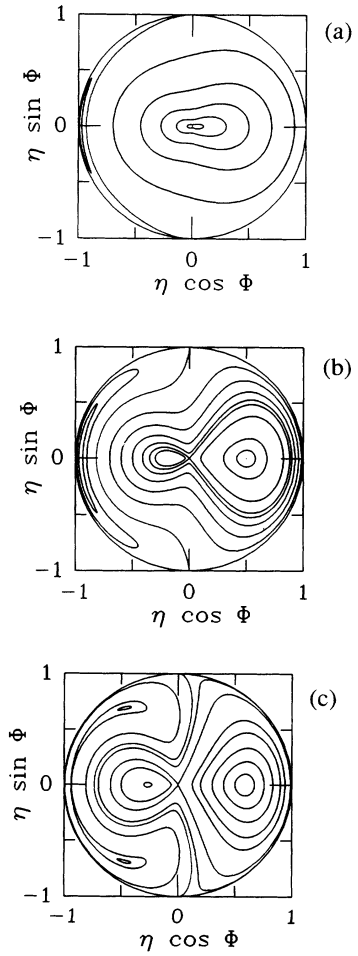

FIG. 4. Trajectories that represent the evolution of the four-wave mixing process in the reduced phase plane $(\eta \cos(\Phi), \eta \sin(\Phi))$, for different values of the linear mismatch $\kappa > 0$ (normal-dispersion regime). (a) $\kappa = 4$; (b) $\kappa = 1$; (c) $\kappa = 0.25$.

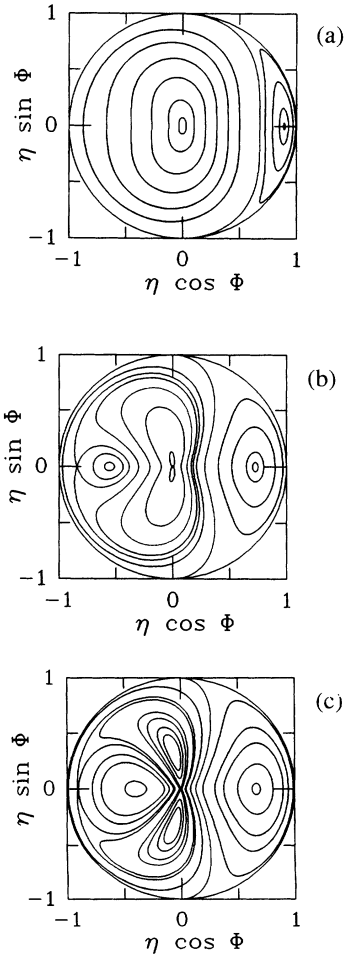

FIG. 5. Same as in Fig. 4, for propagation in the anomalous-dispersion regime (i.e., $\kappa < 0$). (a) $\kappa = -4$; (b) $\kappa = -1.2$; (c) $\kappa = -0.5$.

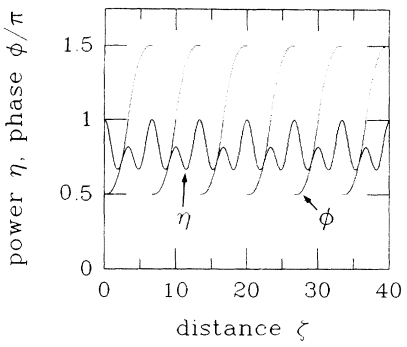

FIG. 6. Evolution with distance ζ of the power η and the phase Φ from dual frequency pumping without a seed, and $\kappa = 1$ [as in Fig. 4(b)].

$\kappa = 0.25$) shows that for $\kappa < 0.5$ also the eigenmode with $(\eta_e \simeq 1, \Phi_e = \pi)$ exchanges its stability with the two new stable centers in Eq. (11) and becomes an unstable saddle (see also Fig. 2). However, as far as the energy conversion between the modes is concerned, this bifurcation only plays a minor role. In fact, the orbits in the neighborhood of the separatrix that emanates from the new saddle point show only small displacements from the circles with $\eta = \text{const}$.

Let us consider now the phase-plane dynamics of Eqs. (7) in the anomalous-dispersion regime. Figure 5(a) shows the level curves of $\tilde{H}$ in a phase-mismatched situation (here $\kappa = -4$). As can be seen, in this case the stable centers are the sideband mode and the eigenmode with $\Phi_e = 0$ that is obtained from Eq. (10). In the absence of instabilities, the energy conversion between the waves is fairly small. As shown in Fig. 5(b), where $\kappa = -1.2$, in the anomalous-dispersion regime the first bifurcation (as the absolute value of the linear mismatch is progressively reduced) occurs for the eigenmode with $\Phi_e = \pi$. Whereas a new stable center with $\Phi_e = \pi$ appears in the phase plane [see Fig. 5(b)].

Finally, Fig. 5(c), where $\kappa = -0.5$, shows the phase-plane dynamics in the case of low mismatch. The bifurcation of the sideband mode (i.e., with $\eta = 0$) into an unstable saddle generates two new symmetric stable centers [see Eq. (11)].

V. MULTIMODE WAVE MIXING

It is important to examine the domain of validity of the four-wave truncation in Eq. (4) by means of comparing the exact solutions and the phase-plane dynamics of Eqs. (7) with the direct numerical solution of Eq. (1) with periodic boundary conditions in time. We have solved Eq. (1) with the frequency symmetric initial condition

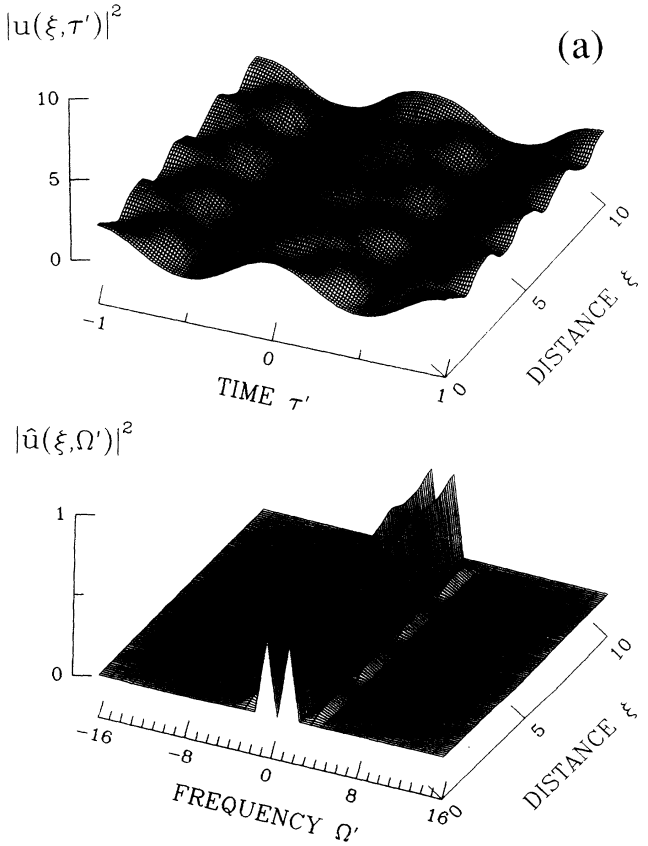

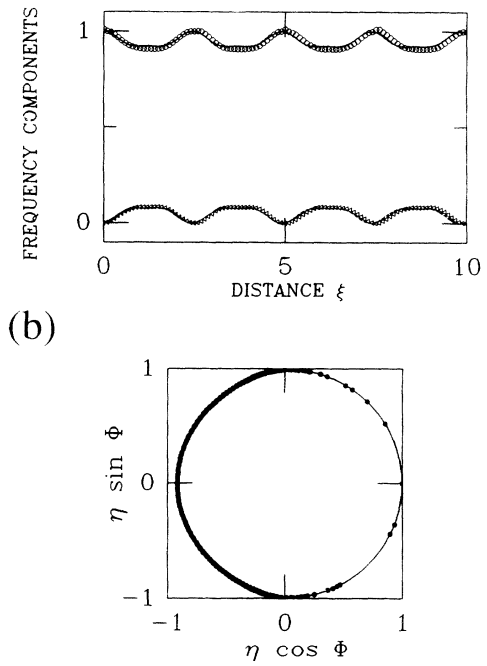

FIG. 7. Numerical solutions of the NLS equation with a four-mode input field as in Eq. (16): (a) temporal evolution of the field, and its power spectrum. The temporal unit is $\tau' = \Omega\tau/\pi$, and the frequency is expressed in units of Ω; (b) power in the pumps (open circles) and in the first-order sidebands (open triangles), and projection from the field $u(\xi,\tau)$ on trajectories in the phase plane $(\eta \sin\Phi, \eta\cos\Phi)$ (dots). The solid and dashed lines indicate the corresponding powers and trajectories that are obtained from the truncated two-mode approximation. Here the initial condition is $\eta(\zeta = 0) = 0.9998$, and $\Phi(\zeta = 0) = 0$, whereas $\kappa = 4$ (normal-dispersion regime).

$$u(\xi=0,\tau)=\epsilon_0+\epsilon_1 e^{i\Phi_1}\cos(\Omega\tau)+\epsilon_2 e^{i\Phi_2}\cos(3\Omega\tau), \tag{16}$$

where ϵ_0 is a weak seed at the mean frequency ω_0. Without loss of generality, throughout this section we fix the (conserved) total energy of the field $P_t = 1$, so that $\xi = \zeta$. Therefore the mismatch in Eqs. (7) reads $\kappa = 8\,\mathrm{sgn}(k'')\Omega^2$. By neglecting for the moment the seed ϵ_0, one obtains from Eq. (16) that $P_t = \epsilon_1^2/2 + \epsilon_2^2/2$. Moreover, $\eta(\xi=0) = \epsilon_1^2/(\epsilon_1^2+\epsilon_2^2) = \epsilon_1^2/2$, and $\Phi(\xi = 0) = \Phi_1 - \Phi_2$. Note that results similar to those discussed in what follows may be obtained for the antisymmetric ansatz, which is obtained by replacing the cosines with sines in Eq. (16).

For $\epsilon_0 \neq 0$, $\epsilon_1 \ll \epsilon_0$, and $\epsilon_2 = 0$, the initial condition of Eq. (16) is the same ansatz that is used in the study of the modulational instability [in the anomalous-dispersion or focusing regime, i.e., for $\mathrm{sgn}(k'') < 0$] of a single pump wave at frequency ω_0 [17,18,21,22,16]. There is a body of literature which attests to the homoclinic boundaries in the focusing NLS equation, which become apparent in such investigations. The well known modulational instability is nothing but the linearization of the stable and unstable manifolds that emanate from the unstable pump mode at frequency ω_0. As discussed in Ref. [22], great care is required in the choice of a numerical algorithm which respects the homoclinic structure. In fact, an injudicious choice of the discretization, such as for example with the conventional split step Fourier or beam propagation method, may cause the trajectories to wander across the separatrix leading to numerically induced chaos [22]. This of course is inconsistent with the complete integrability of the NLS equation, and may be circumvented by solving Eq. (1) with the integrable Ablowitz-Ladik discretization scheme [22].

Consider now the positive-dispersion regime, where the self-adjointness of the scattering problem that is associated with the NLS equation leads to a real spectrum and the absence of a homoclinic structure for the PDE (1). Nevertheless, as we have seen, truncated four-mode and multimode models of the type of Eq. (3) predict homoclinic instabilities and irregular exchange of energy between the modes as the input optical power is increased (or the frequency separation or dispersive mismatch between the waves is decreased) [27,26]. A numerical study of the effect of the size $2K+1$ of the truncation

$$u(\xi,\tau)=\sum_{m=-K}^{K} A_m(\xi)e^{-im\Omega\tau} \tag{17}$$

of the solutions of Eq. (1) showed, by means of the numerical calculation of the unstable Lyapunov exponents,

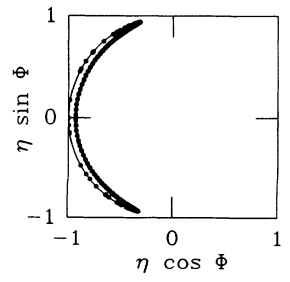

FIG. 8. Phase-plane projections from the numerically computed pump and first sideband components of the field u as in Fig. 7(b), with $\Phi(\zeta=0)=\pi$.

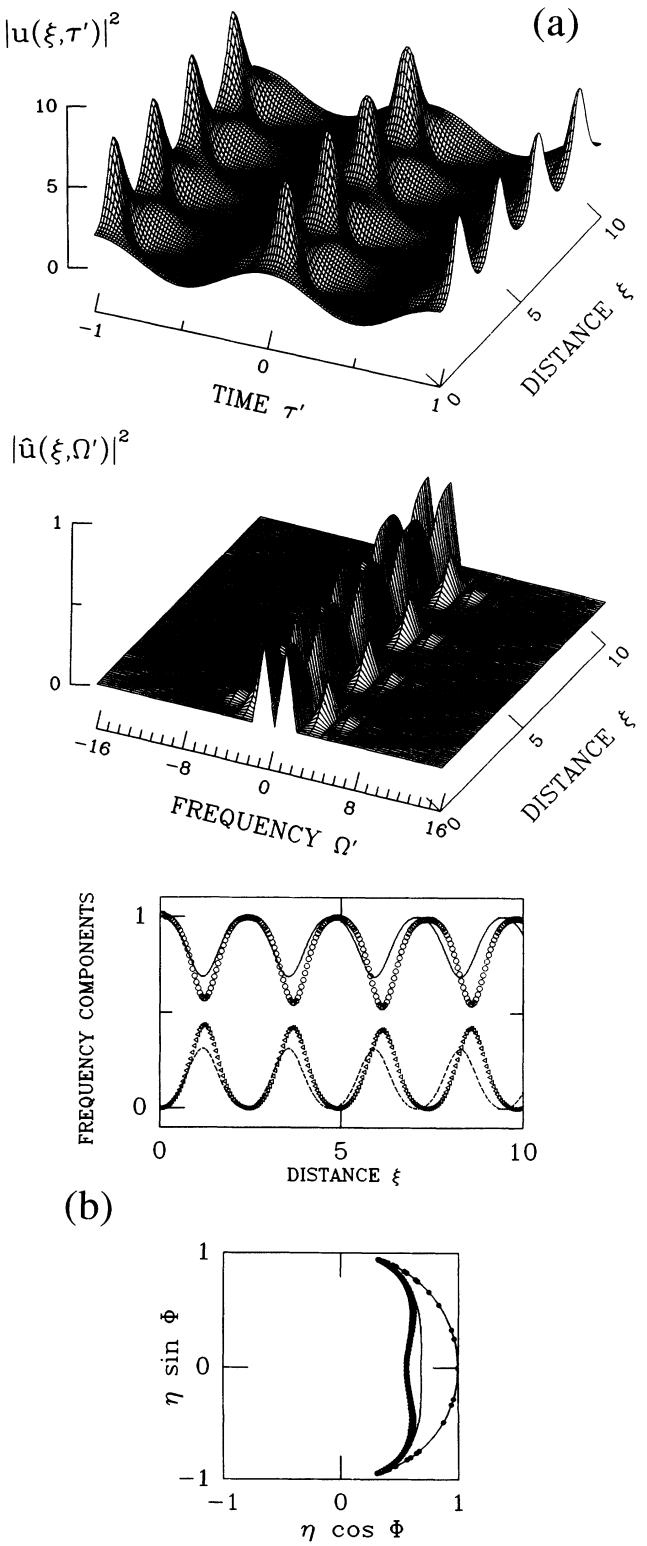

FIG. 9. Same as in Fig. 7, with $\kappa = -4$ (anomalous-dispersion regime).

that the chaotic behavior which occurs in the resulting coupled ODE's for the complex amplitudes A_m tends to vanish as $K \to \infty$ [33]. This result demonstrates that the solutions of Eq. (1) are complex and multiperiodic but not strictly chaotic, so that spatial chaos is artificially introduced by the truncation to a finite number $2K+1$ of sidebands. The quasiperiodic behavior in the multiwave mixing process has been recently analyzed by computing the direct spectral transform of the regular and irregular solutions of the periodic NLS equation [34]. Clearly, chaotic behavior may still be easily introduced in a real physical situation whenever a perturbation to the integrable Eq. (1) is present, e.g., by including higher-order nonlinear and dispersive terms or with periodic amplification.

We also wish to point out that Eq. (16) with $\epsilon_0 \neq 0$, $|\epsilon_0| \ll \epsilon_1$, and $\epsilon_2 = 0$, provides the same initial conditions that were used in Ref. [39] in order to predict the modulational instability of two pump waves with a frequency separation 2Ω. This instability leads to the parametric growth of an initially weak seed at the frequency $\omega = 0$ that is intermediate between the pumps. Note that, in this mixing process, gain for the seed is predicted in the normal-dispersion regime of the fiber. Moreover, the nonlinear dynamics of three-wave mixing, i.e., in the regime of pump depletion (but neglecting four-wave mixing), was discussed in detail in Ref. [40]. However, contrary to the predictions of the truncated three-wave model, in the numerical simulations we found out that the parametric growth of the weak seed at $\omega = 0$ is not observed. In fact, four-wave mixing prevails and as a result the sidebands at frequencies $\pm 3\Omega$ grow along the fiber, even in the case where $\epsilon_0 \neq 0$, $\epsilon_0 \ll \epsilon_1$, $\epsilon_2 = 0$, and where the frequency detuning Ω is chosen in such a way to optimize the modulational instability gain of the seed. As a consequence, we will limit ourselves to analyzing the nonlinear wave mixing dynamics with $\epsilon_0 = 0$ in the initial conditions (16).

Figure 7 and following figures show the result of the numerical integration of the Ablowitz-Ladik discretization scheme of the NLS equation (1). In Fig. 7(a) we show the temporal and spectral evolution of the field versus the dimensionless distance ξ. In the figures, the temporal unit is $\tau' = \Omega\tau/\pi$, and the frequency is expressed in units of Ω. Whereas in Fig. 7(b) we display the power in the pumps (open circles) and in the first order sidebands (open triangles), and the projection from the field $u(\xi,\tau)$ onto the trajectories of the phase plane $(\eta \sin\Phi, \eta\cos\Phi)$ (dots). In the simulations, we keep the initial power ratio between the pumps and the first sidebands fixed [i.e., $\eta(\zeta = 0) = 0.9998$, or $\epsilon_1 \simeq \sqrt{2}$, and $\epsilon_2 = 0.02$], whereas

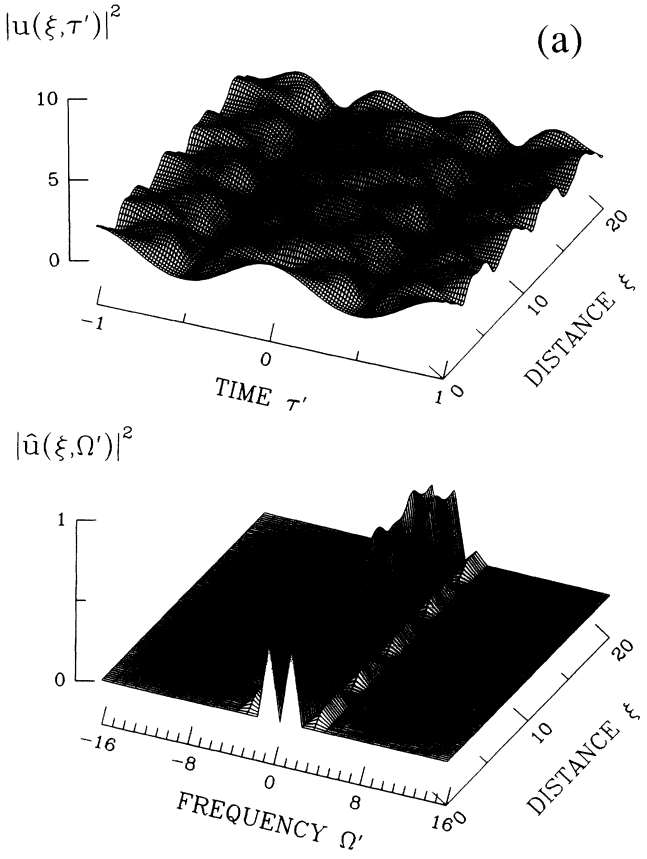

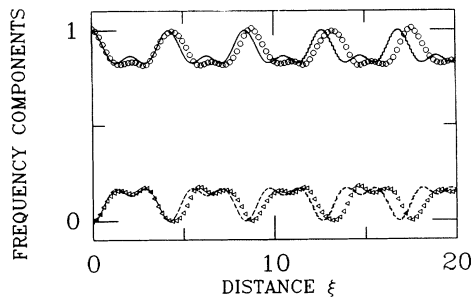

(b)

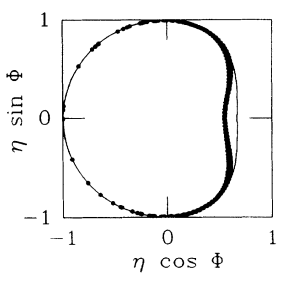

FIG. 10. Same as in Fig. 8, with $\kappa = -4$, and $\Phi(\zeta = 0) = \pi$.

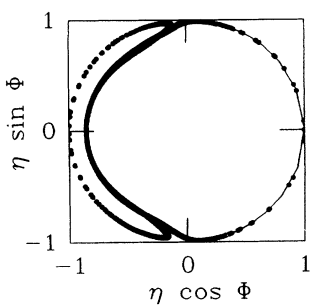

FIG. 11. Same as in Fig. 7, with $\kappa = 2$.

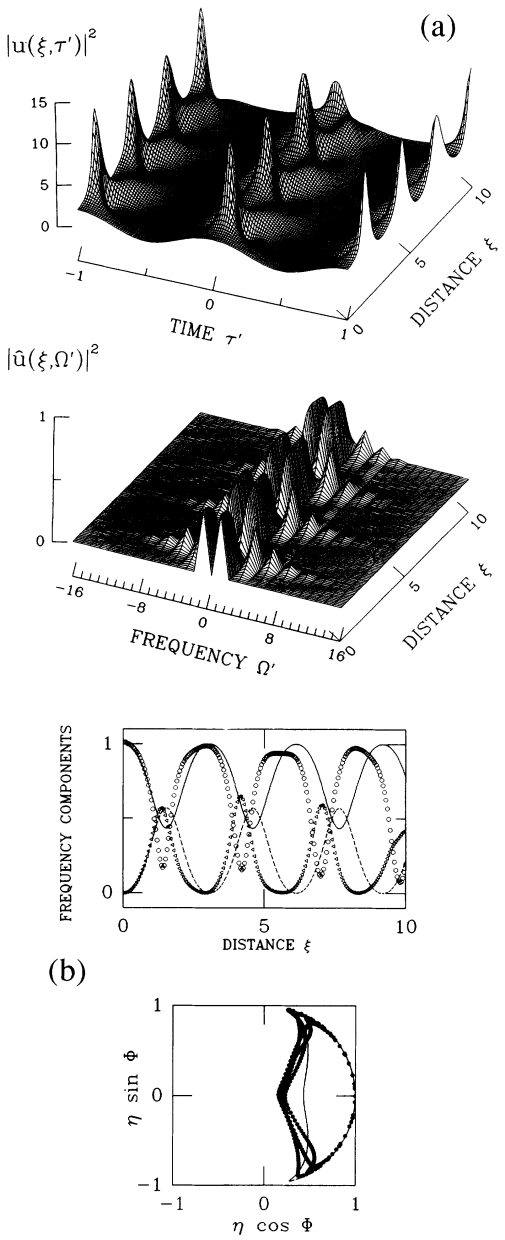

FIG. 12. Same as in Fig. 9, with $\kappa = -2$.

$\Phi(\zeta = 0) = 0, \pi$. Here we set $\Phi(\zeta = 0) = 0$ and the linear mismatch $\kappa = 4$, i.e., the waves propagate in the normal-dispersion regime of the fiber. In order to demonstrate the validity of the two-mode truncation, in Fig. 7(b) we also show the evolution of power in the pumps (solid line) and in the sidebands (dashed line), as well as the phase-plane trajectory (solid line), that are obtained from the exact solution of Eqs. (7).

As can be seen in Fig. 7, with relatively high values of the linear mismatch κ there is only a small energy conversion (i.e., less than 10%) from the pumps to the first sidebands, and virtually no energy is transfered into the higher-order sidebands. As one would expect, in this case the phase-space plot in Fig. 7(b) that is obtained

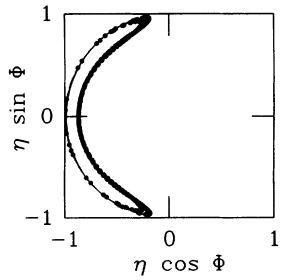

FIG. 13. Same as in Fig. 8, with $\kappa = 2$, and $\Phi(\zeta = 0) = \pi$.

from the numerically computed Fourier components of the field u closely follows a trajectory of the truncated two-mode approximation [see also Fig. 4(a)]. Note that here and in the following phase-plane plots, the numerically computed η coordinate is calculated as the energy ratio between the pumps and the first sidebands only, that is we do not consider the energy that is coupled into the higher order sidemodes in the solutions of the NLS equation.

Figure 8 shows the projection on the phase plane of the numerical solution of the NLS equation with the same input condition as in Fig. 7 but with $\Phi(\zeta = 0) = \pi$. As can be seen by comparing the numerical projection (dots) with the exact trajectory (solid line), also in this case there is a good agreement between the dynamics of the truncated model and that of the multiwave mixing.

On the other hand Fig. 9 shows that for $\kappa = -4$, that is in the anomalous-dispersion regime, the maximum energy depletion of the pumps is of about 45%, out of which approximately 5% is coupled into the higher-order sidebands [here $\Phi(\zeta = 0) = \pi$]. Nevertheless, by comparing the phase-plane projection of Fig. 9(b) and Fig. 10 [here $\kappa = -4$ and $\Phi(\zeta = 0) = \pi$] with the truncated two-mode trajectories [see also Fig. 5(a)], one still finds a good qualitative agreement between the predictions of the two-mode truncation and the numerical solution of the NLS equation. In fact, by inspecting the exact trajectories of the phase-plane plot [5(a)] one immediately observes the larger depletion of the pumps from the much closer approach to the origin of the trajectories that pass near the circle $\eta = 1$ with respect to the same curves in the phase portrait [4(a)].

Moreover, the information about the relative phase between the pumps and the sidebands that is provided by

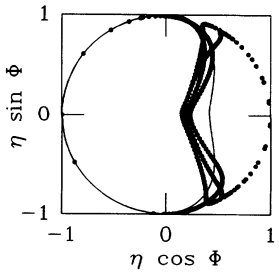

FIG. 14. Same as in Fig. 8, with $\kappa = -2$, and $\Phi(\zeta = 0) = \pi$.

the phase-plane projections gives a useful insight for understanding the origin of the temporal compression that is observed in the periodic pulse trains that form in the anomalous-dispersion regime [see Fig. 9(a)]. Whereas in the case of propagation in the normal-dispersion regime [see Fig. 7(a)] no distinct pulse train is formed. In fact, Fig. 9(b) shows that at the point where maximum pump depletion occurs, the pumps and the first sidebands add up in phase. By induction, we may conjecture that all the sidemodes also add up in phase for $\tau = 0$, which explains the periodic temporal compression into pulse trains of Fig. 9(a). On the other hand, Fig. 7(b) shows that in the normal-dispersion regime the pumps and the generated sidebands are precisely π out of phase at the point

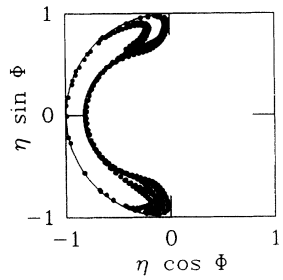

FIG. 16. Same as in Fig. 8, with $\kappa = 1$, and $\Phi(\zeta = 0) = \pi$.

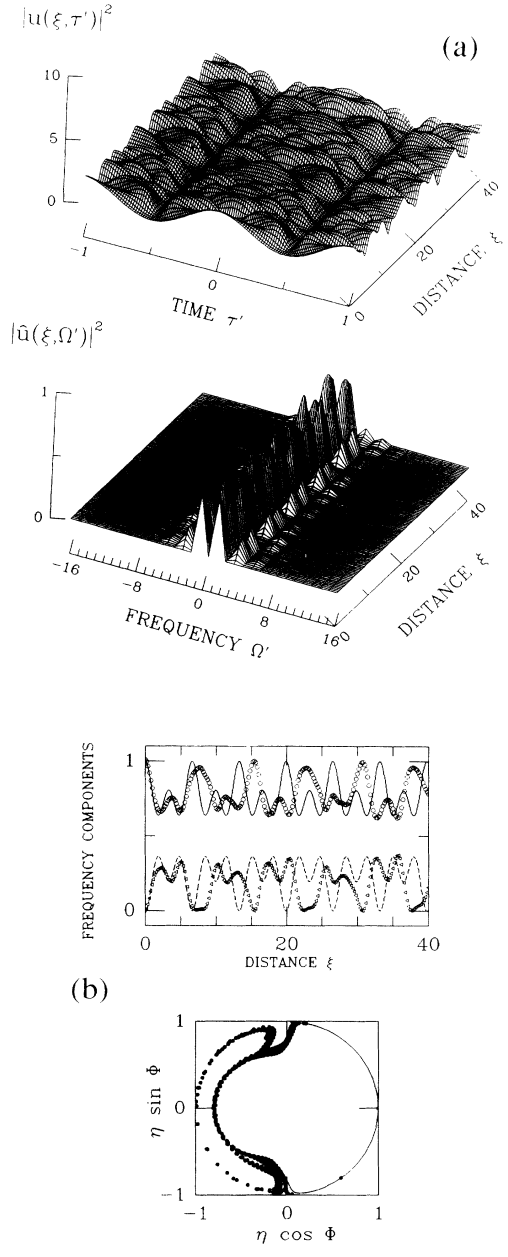

FIG. 15. Same as in Fig. 7, with $\kappa = 1$.

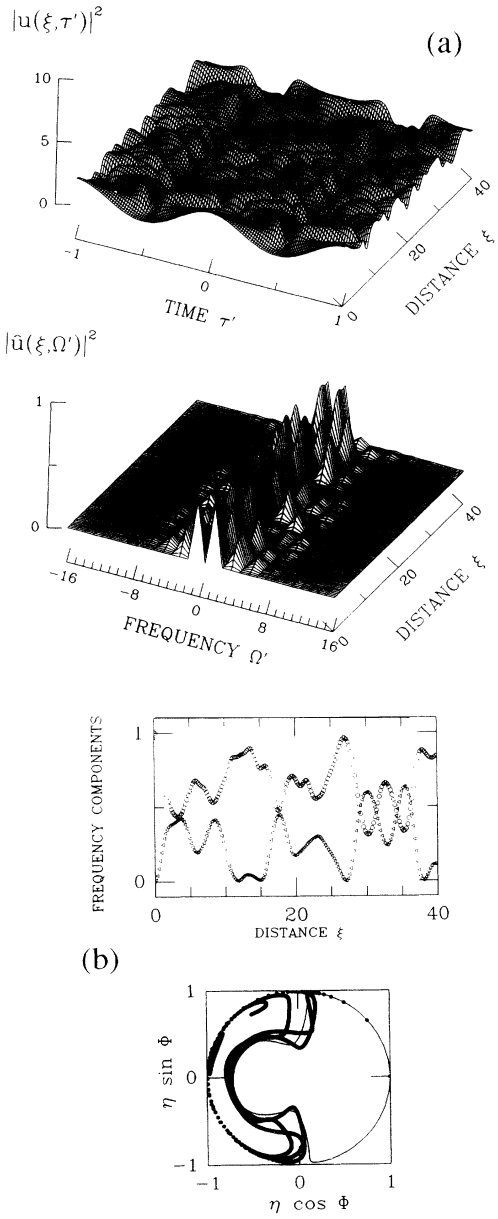

FIG. 17. Same as in Fig. 7, with $\kappa = 0.5$.

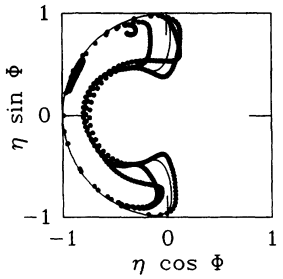

FIG. 18. Same as in Fig. 8, with $\kappa = 0.5$, and $\Phi(\zeta = 0) = \pi$.

of maximum pump depletion, hence one obtains a low contrast ratio in the periodic wave trains in Fig. 7(a).

Let us consider now the effects of progressively decreasing the absolute value of the linear mismatch κ. Reducing the linear mismatch enhances the transfer of energy from the pumps into the sidebands in the sense that both the pump depletion and the number of generated higher-order sidebands increase. As one would expect, whenever a significant portion of the initial energy gets coupled into a relatively large number of modes, the action of these modes tends to unlock the simple integrable dynamics of the two-mode truncation. As a consequence, a complex or irregular behavior is expected to appear in the spectral redistribution of energy along the fiber. As we shall see, in order to establish more precisely the irregular character of the full solutions of the NLS equation, we project these numerical solutions on the phase plane in order to obtain an immediate visual insight that would otherwise be unavailable from the simple inspection of the temporal and spectral evolutions of the field u.

Figures 11 and 12 show the temporal and spectral evolution of the field u as well as its phase portrait for $\kappa = 2$ and $\kappa = -2$, respectively, where $\Phi(\zeta = 0) = 0$. As can be seen, in the normal-dispersion regime there is still a negligible fraction of energy that is coupled outside the initially excited four waves, and the resulting dynamics is essentially locked onto the integrable trajectories of the truncated model. In particular, note from Figs. 11(b) and 13 [with $\Phi(\zeta = 0) = \pi$] that a good agreement exists both in the shape and in the period of the energy exchange curves from the two mode predictions and the numerical solutions of the NLS equation. Note, however, from Fig. 11(b) that the projection of the field u does not exactly follow a single trajectory on the phase plane. Rather, there is a moderate spread of trajectories that shows up in the projection as an irregular jumping between the two domains of Fig. 11(b). In the anomalous-dispersion regime with $\kappa = -2$, Figs. 12(b) and 14 show larger widths with respect to the $\kappa = 2$ case for the range of nearby trajectories that result from the projection of the NLS solutions. The diagram for the energy transfer in 12(b) first shows the appearance of a slightly quasiperiodic behavior. Note that in this case the periodic depletion of the pumps is almost complete, whereas about 20% of the energy is coupled to higher-order sidemodes. This demonstrates that even in this rather extreme situation the dynamics of the energy exchange between the pumps and the first-order sidebands is still fairly well reproduced by the exact solutions of the two-mode truncation.

Whenever the value of $|\kappa|$ is reduced even further, the higher-order modes actively participate to the process of energy exchange along the fiber and irregular or quasiperiodic evolutions result. In the normal-dispersion regime, the transition to irregular behavior is illustrated by the comparison of Figs. 15 and 16 (that have been obtained with $\kappa = 1$ and $\Phi = 0, \pi$, respectively) with Figs. 17 and 18 (where κ is reduced down to 0.5). As can be seen from Fig. 17(b), in this last case a seemingly aperiodic spatial evolution of energy in the spectral

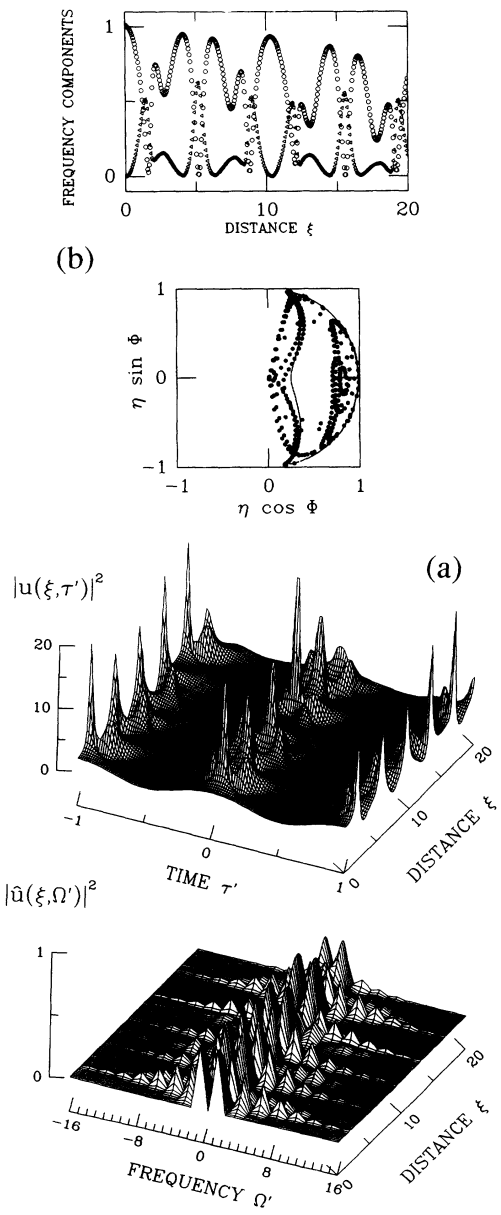

FIG. 19. Same as in Fig. 9, with $\kappa = -1$. Here the evolutions of power in the pumps and sidebands that are obtained from the truncated model are not indicated.

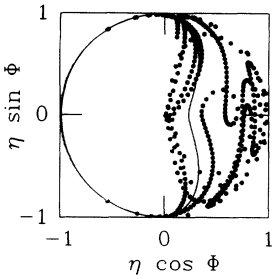

FIG. 20. Same as in Fig. 8, with $\kappa = -1$, and $\Phi(\zeta = 0) = \pi$.

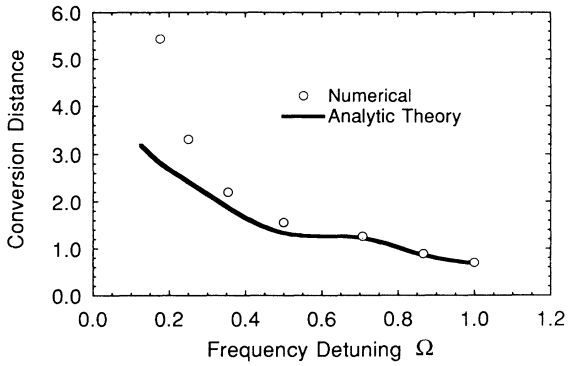

FIG. 21. Frequency conversion distance Z_c (in units of the dispersion length z_0) versus the normalized frequency separation Ω, in the normal-dispersion regime of the fiber. Solid line: prediction of the truncated exactly solvable model. Dots: from the numerical solutions of the NLS equation.

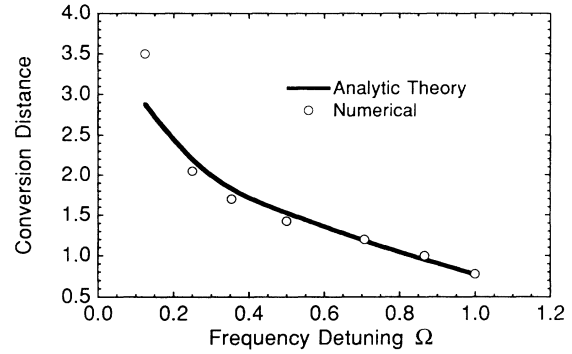

FIG. 22. Same as in Fig. 21, in the anomalous-dispersion regime of the fiber.

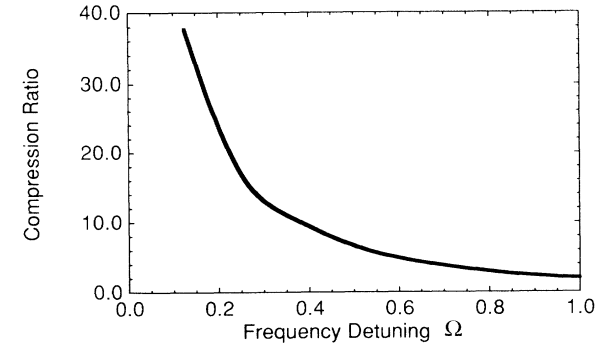

FIG. 23. Maximum compression ratio (at $Z = Z_c$) versus the normalized frequency separation Ω, in the anomalous-dispersion regime of the fiber.

components of the field results. However, it is quite remarkable that the projections of the field u on the phase plane still tend to mimic to a certain extent the trajectories of the two-mode approximation. This indicates that in some sense the information that is provided by the phase portrait is more robust to higher-order sideband perturbations than it is the value of the spatial period of energy exchange.

In the anomalous-dispersion regime a much stronger transition to spatially irregular multiwave mixing is observed, as can be seen from the plots of Figs. 19 and 20, where $\kappa = -1$ and $\Phi(\xi = 0) = 0$ or π, respectively. In fact, in this case both the period of depletion of the pumps as well as the phase-space trajectories appear to wander in a highly erratic fashion.

VI. APPLICATIONS

In this section we briefly discuss by means of some specific examples the conditions for the experimental observability of the wave conversion phenomena that we presented above. An important parameter that may be extracted from our analysis is the distance, say, Z_c [in the dimensionless units of Eq. (1)], where the maximum conversion from the pump into the sidebands first occurs. This distance may be easily obtained from the exact solutions of Eqs. (5) or Eqs. (7). The solid lines in Figs. 21 and 22 show the dependence of the conversion distance Z_c (that is obtained from the present truncated model) on the dimensionless frequency separation Ω, in the case of propagation in the normal- and in the anomalous-dispersion regime, respectively. The dots indicate the corresponding values of the conversion distance that are obtained from the numerical solution of the NLS equation (1). As can be seen, there is a good agreement, as far as the estimation of Z_c is concerned, between the approximated truncated four-wave model and the solutions of the full PDE model, at least for frequencies Ω larger than a certain critical value, say, Ω_c. In both cases of normal or anomalous dispersion, the results in the figures show that $\Omega_c \simeq 0.3$.

Let us translate these results to real physical units in order to understand the relevance of the four-wave mixing process in different experimental situations. From the actual value of the pump frequency separation, say, Δf(GHz), and the dimensionless value of Ω, one obtains the time scale t_0(nsec)$= \Omega/(\pi \Delta f)$. This parameter in turn determines the dispersion distance $z_0 = t_0^2/|k''|$. Whenever the input dimensionless power in each of the pumps is equal to 1/2, the real pump power is $P = |k''|/(2t_0^2 R)$, where $R = 2\pi n_2/(\lambda A)$, λ is the wavelength, and A is the fiber effective area.

Consider for example the case of propagation in the normal-dispersion regime. With reference to the experiments in Refs. [30–32], where the dynamics of the dual-frequency-pumped wave mixing in a fiber was investi-

gated by means of two pulsed dye lasers at the wavelength of 630 nm with frequency spacings of 10–20 cm^{-1} (300–600 GHz), the condition $\Omega = 1$ and the fiber dispersion $k'' = 70$ ps^2/km lead to $z_0 = 15.5$–3.9 m. From Fig. 21, one obtains that the conversion distance is equal to $Z_c z_0 = 10.7$–2.7 m, respectively. With an effective area of $A = 1.8 \times 10^{-11}$ m^2, one obtains that the optical power in the fiber from each pump laser is equal to 3.7 or 7.3 W, respectively. In the case of Ref. [9], strong four-wave mixing conversion was observed by means of four-wave mixing of pulsed light from an argon laser ($\lambda = 514$ nm) that operated on two longitudinal modes (spaced by 2.1 GHz). With $\Omega = 0.18$ and the group-velocity dispersion of 62 ps^2/m, one obtains $z_0 = 11$ km, and the conversion distance (from Fig. 21) is equal to 61 km, for a total input power in the fiber of 3.5 mW.

On the other hand, the impact of the four-wave mixing effects that we discussed here as a potential source of degradation of the performances of lightwave transmission systems may be appreciated by considering the case of a dispersion shifted fiber [8]. In fact, the nonlinear interaction of two adjacent wavelength channels may set a lower bound to their frequency separation. For example, in the case of two 2.5 Gbit/s channels that are separated by 12.5 GHz, the dispersion $k'' = 1.3$ ps^2/km and $\Omega = 1$ yield $z_0 = 52$ km, and the conversion distance is 36 km, with an input power of about 3 mW from each channel. Note that in a system with periodic lumped amplification [7] the conversion efficiency of the four-wave mixing process may be enhanced by resonance effects whenever the amplifier spacing is of the order of the conversion distance.

As we have seen in the preceding section, in the case of propagation in the anomalous-dispersion regime the creation of high-order sidebands along the fiber is accompanied by a strong compression in time of the initial sinusoidal wave form. This temporal compression has a recursive behavior with the distance Z, therefore for a given fiber length one obtains a maximum degree of compression at a certain fixed value of the pump power. Let us briefly discuss the potential of this effect for the creation of a high repetition rate soliton source. Figure

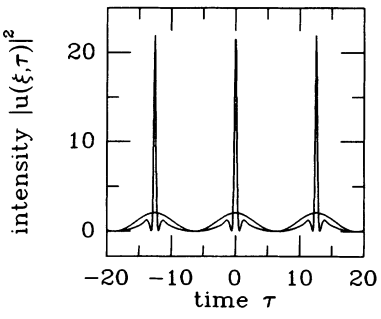

FIG. 24. Initial and compressed (at $Z = Z_c$) temporal profiles of the periodic signal in the fiber operating in the anomalous-dispersion regime.

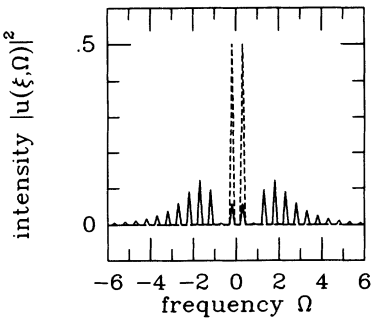

FIG. 25. Frequency spectra that correspond to the temporal envelopes in Fig. 24.

23 illustrates the compression ratio, that is the ratio between the time width of the initial sinusoidal train and the width of the compressed pulses that forms at the distance Z_c. As can be seen, whenever the input frequency separation Ω grows smaller than 0.5 one may obtain relatively large compression ratios. As it is shown in Figs. 24 and 25, the compressed pulses sit on low power wings which could be eliminated by means of an intensity discriminator such as for example a birefringent fiber and a polarizer [41]. Note that another approach to produce a pedestal-free train of compressed soliton pulses from the mixing in a fiber of a dual frequency signal may involve the inclusion of a dissipative mechanism such as adiabatic amplification (or equivalently, varying dispersion) along the fiber [42,43]. In the present case of a uniform, ideally loss-free fiber, the generation of a pulse train with a 100 GHz repetition rate and a compression factor of about 10 is obtained for $\Omega \simeq 0.4$ (see Fig. 23). With the fiber dispersion $k'' = 1.4$ ps^2/km, the results of Fig. 22 show that the conversion (or compression) distance is equal to 1.1 km for an input power from each pump laser of 150 mW.

VII. CONCLUSIONS

We have studied the exactly integrable nonlinear dynamics of the nonlinear mixing between four symmetric or antisymmetric waves (i.e., two independent modes) in the normal- and anomalous-dispersion regime of a single-mode optical fiber. We have examined the validity of the truncated model, that neglects the back action of higher-order generated sidebands, by comparing the exact solutions of the two-mode equations with the numerical solutions of the NLS equation with periodic boundary conditions. We found that the two-mode truncation may provide a fairly good description of the dual-frequency-pumped wave mixing process even in the strong depletion regime of the pumps, provided that the linear mismatch is relatively high so that the energy exchange between the waves is almost periodic along the fiber.

Whenever the absolute value of the linear mismatch $|\kappa|$ is small, the dynamics of the truncated two-mode equations exhibits several bifurcation and instability phenom-

ena. These instabilities are peculiar to the truncation in the sense that they may have no counterpart in the higher dimensional phase-space dynamics of the coupled ODE's that are obtained as more and more sidebands are kept into the count [e.g., $K \to \infty$ in Eq. (17)]. Take for example the normal-dispersion regime, where there are no instabilities and no homoclinic solutions of the NLS equation (1), which is the infinite dimensional limit of the set of coupled multiwave mixing ODE's. Nevertheless, we found that for low mismatches the projections on the truncated phase plane of the numerical solutions of NLS equation show a complex multiperiodic behavior in the power exchange among the frequency components along the propagation coordinate. We may therefore view the bifurcation and spatial instability effects of the simple two-mode truncated model that we have considered here as the signature of the spatiotemporal complexity of the solutions of the NLS equation. We have also briefly outlined the conditions for the experimental observation of strong frequency conversion from the multiwave mixing in fibers, with particular relevance to applications such as wavelength division multiplexed transmissions and high repetition rate pulse train generation.

ACKNOWLEDGMENTS

We thank C. West for help in understanding the connection between the nonlinear eigenmodes of the truncated two-wave mixing model and the phase-locked exact solutions of the NLS equation. The work of S. T. and S. W. was carried out in the framework of the agreement between the Fondazione Ugo Bordoni and the Istituto Superiore Poste e Telecomunicazioni.

[1] K. O. Hill, D. C. Johnson, B. S. Kawasaki, and R. I. MacDonald, J. Appl. Phys. **49**, 5098 (1987).
[2] R. H. Stolen, and J. E. Bjorkholm, IEEE J. Quantum Electron. **QE-18**, 1062 (1982).
[3] R. H. Stolen, *Optical Fiber Telecommunications* (Academic, New York, 1979), pp. 125–150.
[4] N. Shibata, R. P. Braun, and R. G. Waarts, IEEE J. Quantum Electron. **23**, 1205 (1987).
[5] R. G. Waarts and R. P. Braun, Electron. Lett. **22**, 873 (1986).
[6] K. Inoue, H. Toba, and K. Oda, J. Lightwave Technol. **10**, 350 (1992).
[7] D. G. Schadt, Electron. Lett. **27**, 1805 (1991).
[8] D. A. Cleland, X. Y. Gu, J. D. Cox, and A. D. Ellis, Electron. Lett. **28**, 307 (1992).
[9] H. H. Yaffe, R. G. Waarts, E. Lichtman, and A. A. Friesem, Electron. Lett. **23**, 42 (1987).
[10] E. Lichtman, A. A. Friesem, R. G. Waarts, and H. H. Yaffe, J. Opt. Soc. Am. B **11**, 1801 (1988).
[11] E. Lichtman, A. A. Friesem, S. Tang, and R. G. Waarts, J. Lightwave Technol. **9**, 422 (1991).
[12] V. E. Zakharov and A. B. Shabat, Zh. Eksp. Teor. Fiz. **61**, 118 (1971) [Sov. Phys. JETP **34**, 62 (1972)].
[13] Y. Ma and M. J. Ablowitz, SIAM Stud. Appl. Math. **65**, 113 (1981).
[14] E. Infeld and G. Rowlands, *Nonlinear Waves, Solitons and Chaos* (Cambridge University Press, Cambridge, England, 1990).
[15] E. Infeld, Phys. Rev. Lett. **47**, 717 (1981).
[16] A. R. Bishop, M. G. Forest, D. W. McLaughlin, and E. A. Overman, Phys. Lett. A **144**, 17 (1990).
[17] S. Trillo and S. Wabnitz, Opt. Lett. **16**, 1566 (1991).
[18] S. Trillo and S. Wabnitz, Opt. Lett. **16**, 986 (1991).
[19] E. R. Tracy, H. H. Chen, and Y. C. Lee, Phys. Rev. Lett. **53**, 218 (1984).
[20] E. R. Tracy and H. H. Chen, Phys. Rev. A **37**, 815 (1988).
[21] N. N. Akhmediev and V. I. Korneev, Theor. Math. Phys. **69**, 1089 (1987) [Teor. Mat. Fiz. **69**, 189 (1986)].
[22] M. J. Ablowitz and B. M. Herbst, SIAM J. Appl. Math. **50**, 339 (1990).
[23] G. Cappellini and S. Trillo, Phys. Rev. A **44**, 7509 (1991).
[24] S. Trillo and S. Wabnitz, Phys. Lett. A **159**, 252 (1991).
[25] M. Haelterman, S. Trillo, and S. Wabnitz, Opt. Lett. **17**, 745 (1992).
[26] S. J. Garth and R. A. Sammut, Opt. Commun. **90**, 311 (1992).
[27] S. Trillo and S. Wabnitz, Phys. Rev. A **36**, 3881 (1987).
[28] N. V. Alekseeva, K. N. Alekseev, V. A. Balueva, G. P. Berman, A. K. Popov, and V. Z. Yakhnin, Opt. Quantum Electron. **23**, 603 (1991).
[29] R. A. Sammut and S. J. Garth, J. Opt. Soc. Am. **8**, 2097 (1991).
[30] J. R. Thompson and R. Roy, Opt. Lett. **16**, 557 (1991).
[31] J. R. Thompson and R. Roy, Phys. Rev. A **43**, 4987 (1991).
[32] J. R. Thompson and R. Roy, Phys. Rev. A **44**, 7605 (1991).
[33] M. M. Shen and D. R. Nicholson, Phys. Fluids **30**, 3150 (1987).
[34] C. S. West and T. A. B. Kennedy, Phys. Rev. A **47**, 1252 (1993).
[35] G. P. Agrawal, Phys. Rev. Lett. **59**, 880 (1987); G. P. Agrawal, P. L. Baldeck, and R. R. Alfano, Phys. Rev. A **39**, 3406 (1989).
[36] T. A. B. Kennedy, S. Trillo, and S. Wabnitz, *Digest of Quantum Electronics and Laser Science (QELS)*, International Conference, Anaheim, California, 1992 (Optical Society of America, Washington, DC, 1992) p. 128.
[37] J. Guckenheimer and P. Holmes, *Nonlinear Oscillations, Dynamical Systems, and Bifurcations of Vector Fields* (Springer, New York, 1983).
[38] I.S. Gradshteyn and I.M. Ryzhik, *Table of Integrals, Se-*

ries, and Products (Academic Press, New York, 1980), p. 911.

[39] A. Barthelemy and R. De La Fuente, Opt. Commun. **73**, 409 (1989).

[40] G. Cappellini and S. Trillo, J. Opt. Soc. Am. B **8**, 824 (1991).

[41] R. H. Stolen, J. Botineau, and A. Ashkin, Opt. Lett. **7**, 512 (1982).

[42] P. V. Mamyshev, S. V. Chernikov, and E. M. Dianov, IEEE J. Quantum Electron. **QE-27**, 2347 (1991).

[43] S. V. Chernikov, J. R. Taylor, P. V. Mamyshev, and E. M. Dianov, Electron. Lett. **28**, 931 (1992).

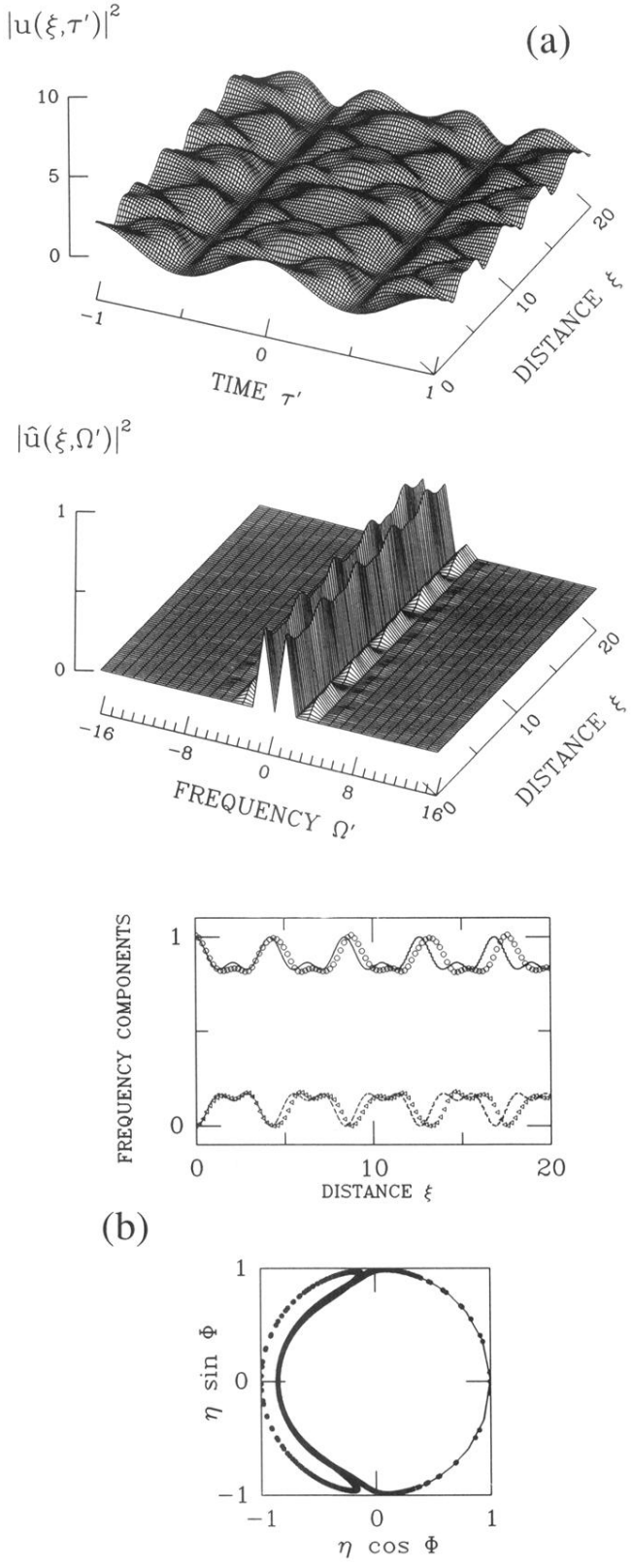

FIG. 11. Same as in Fig. 7, with $\kappa = 2$.

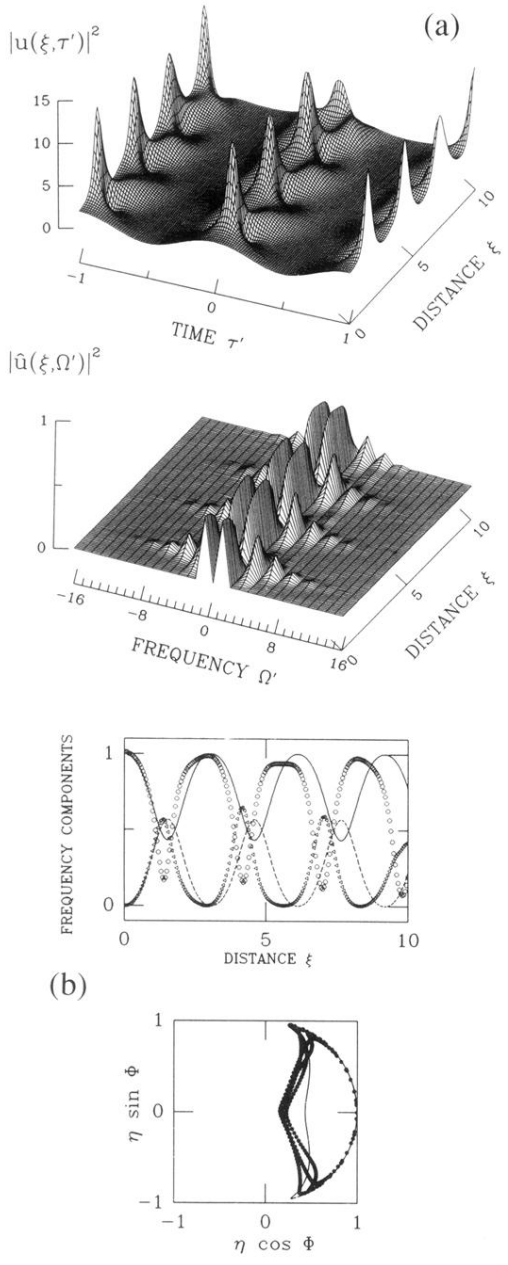

FIG. 12. Same as in Fig. 9, with $\kappa = -2$.

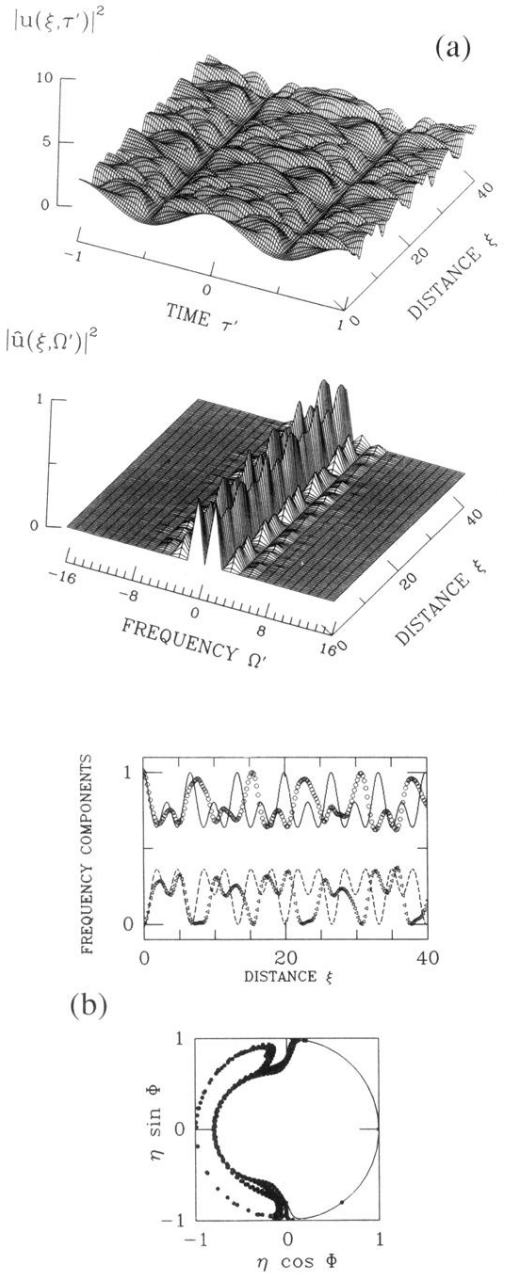

FIG. 15. Same as in Fig. 7, with $\kappa = 1$.

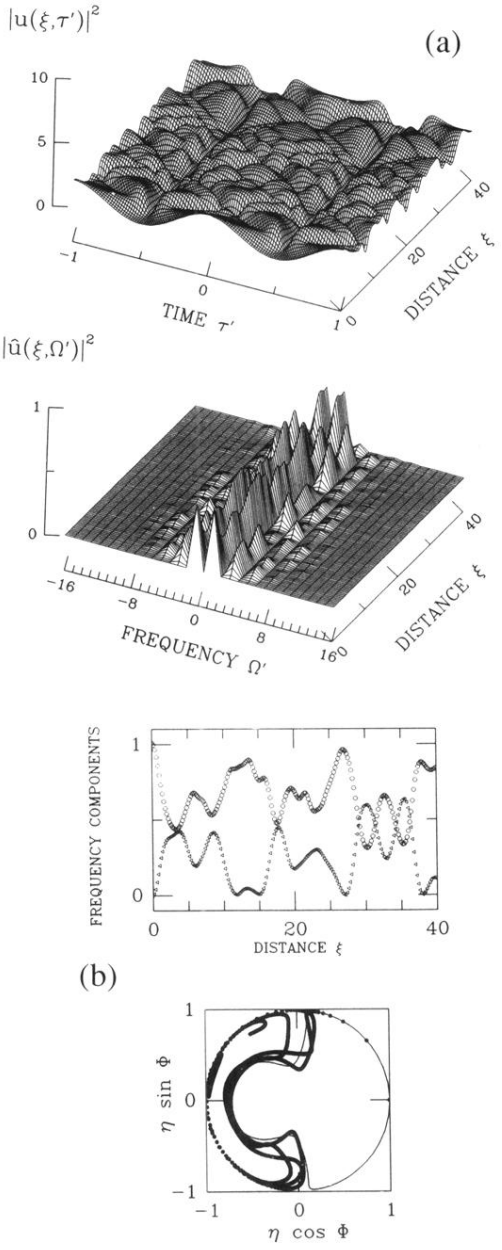

FIG. 17. Same as in Fig. 7, with $\kappa = 0.5$.

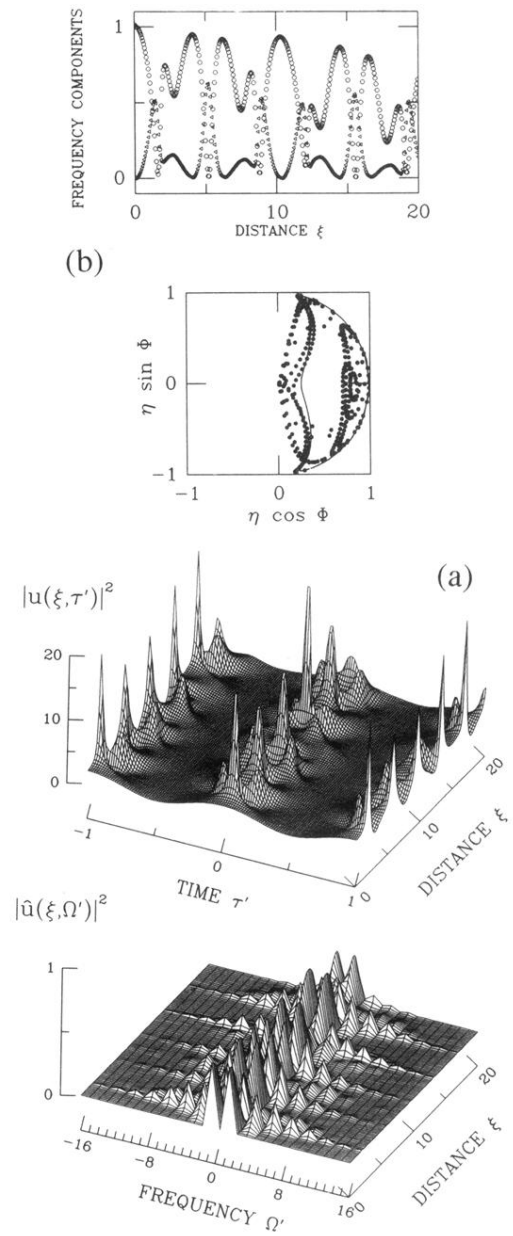

FIG. 19. Same as in Fig. 9, with $\kappa = -1$. Here the evolutions of power in the pumps and sidebands that are obtained from the truncated model are not indicated.

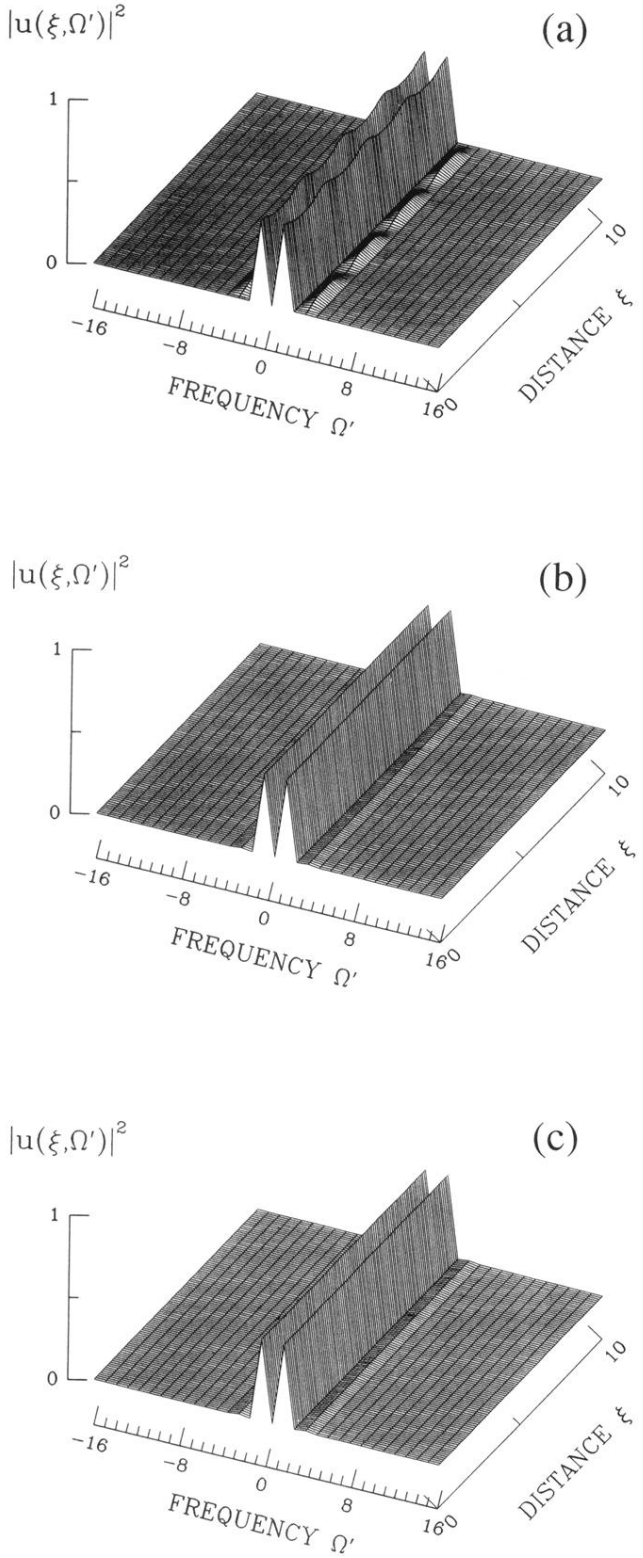

FIG. 3. Power spectrum evolution as obtained from numerical solution of the NLS equation for propagation in the normal-dispersion regime, and $\kappa = 4$. Here the frequency is expressed in units of Ω. (a) In the absence of sideband seed; (b) with initial conditions corresponding to the $\Phi_e = 0$ antisymmetric eigenmode [i.e., the elliptic function sn solution of Eq. (12)]; (c) with initial conditions corresponding to the $\Phi_e = \pi$ symmetric eigenmode [i.e., the elliptic function cd solution of Eq. (13)].

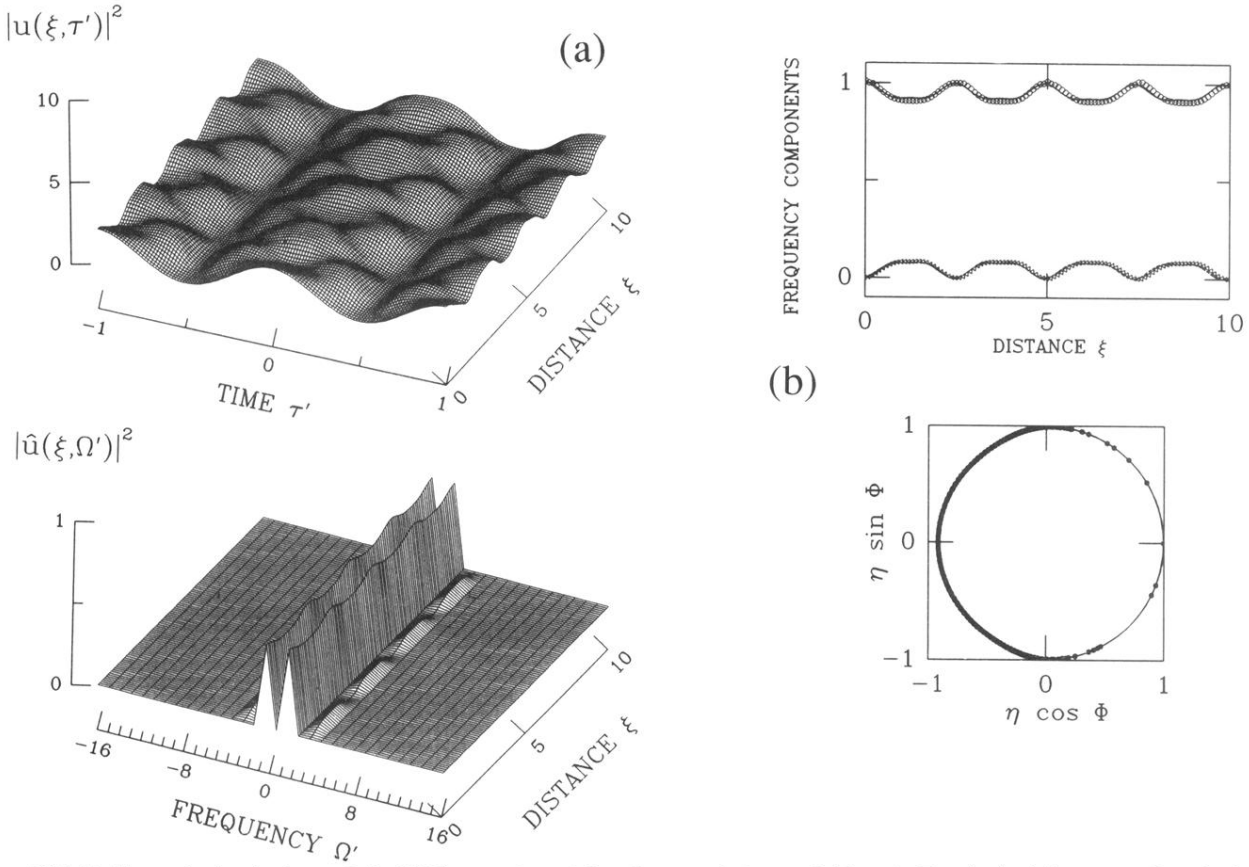

FIG. 7. Numerical solutions of the NLS equation with a four-mode input field as in Eq. (16): (a) temporal evolution of the field, and its power spectrum. The temporal unit is $\tau' = \Omega\tau/\pi$, and the frequency is expressed in units of Ω; (b) power in the pumps (open circles) and in the first-order sidebands (open triangles), and projection from the field $u(\xi, \tau)$ on trajectories in the phase plane $(\eta \sin\Phi, \eta \cos\Phi)$ (dots). The solid and dashed lines indicate the corresponding powers and trajectories that are obtained from the truncated two-mode approximation. Here the initial condition is $\eta(\zeta = 0) = 0.9998$, and $\Phi(\zeta = 0) = 0$, whereas $\kappa = 4$ (normal-dispersion regime).

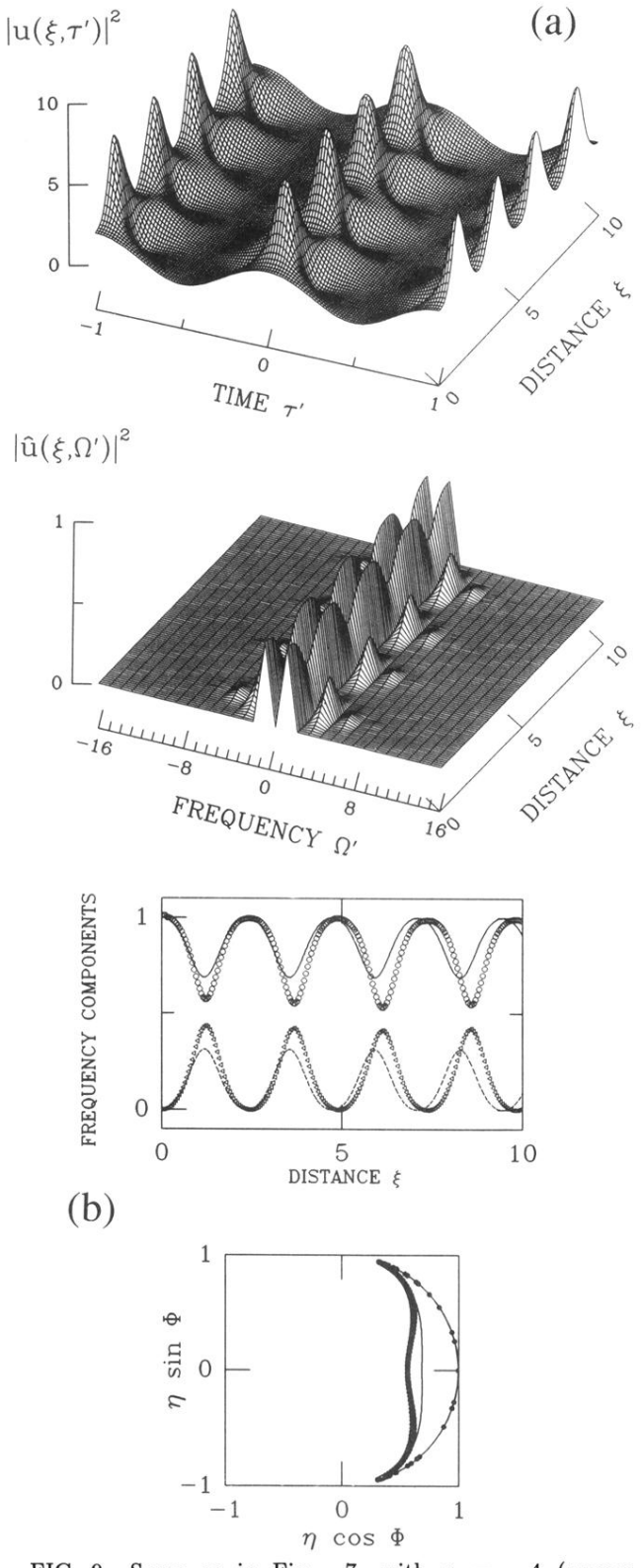

FIG. 9. Same as in Fig. 7, with $\kappa = -4$ (anomalous-dispersion regime).